J. Fluid Mech. (1997), *vol.* 349, *pp.* 327–359. Printed in the United Kingdom

Subharmonic resonance of Venice gates in waves. Part 2. Sinusoidally modulated incident waves

By PAOLO SAMMARCO†, HOANG H. TRAN, ODED GOTTLIEB‡ AND CHIANG C. MEI

Department of Civil and Environmental Engineering,
Massachusetts Institute of Technology, Cambridge, MA, 02139, USA

(Received 11 March 1997 and in revised form 17 June 1997)

In order to examine the effects of finite bandwidth of the incident sea spectrum on the resonance of the articulated storm gates for Venice Lagoon, we consider a narrow band consisting of the carrier frequency and two sidebands. The evolution equation for the gate oscillations now has a time-periodic coefficient, and is equivalent to a non-autonomous dynamical system. For small damping and weak forcing, approximate analysis for local and global bifurcations are carried out, and extended by direct numerical simulation. Typical bifurcation scenarios are also examined by laboratory experiments.

1. Introduction

In Part 1 (Sammarco *et al.* 1997) we have derived the nonlinear evolution equation describing the out-of-phase rotation of Venice gates resonated subharmonically by normally incident waves. The case of uniform amplitude was investigated in detail. Since the frequency band of sea waves in nature is usually finite, we wish to examine in this Part the effects of an idealized narrow band consisting of a slightly detuned central (carrier) frequency $2\omega = 2(\omega_0 + \Delta\omega)$ and two sidebands $2\omega + \Omega$ and $2\omega - \Omega$, with $\Omega = \epsilon^2\Omega_2\omega_0 \ll 1$. The envelope of the incident waves is therefore modulated sinusoidally in time with the period $2\pi/\Omega$

$$A_2 = \overline{A}_2 + \tilde{A}_2 \cos \Omega_2 t_2, \tag{1.1}$$

where $t_2 = \epsilon^2\omega_0 t'$ denotes the dimensionless slow time with t' being the physical time. Since the time derivative of A_2 introduces terms of $O(\epsilon^2)$ smaller than those present, the evolution equation must be

$$-\mathrm{i}\theta_{t_2} = \omega_2\theta + (c_N + \mathrm{i}c_R)\,\theta^2\theta^* + c_F A_2\theta^* + (1+\mathrm{i})\,\delta_2 c_L\theta + \mathrm{i}c_Q|\theta|\theta. \tag{1.2}$$

with A_2 depending on time through (1.1). In terms of physical quantities the extended evolution equation is

$$-\frac{\mathrm{i}}{\omega_0}\theta'_{t'} = \frac{\Delta\omega}{\omega_0}\theta' + (c_N + \mathrm{i}c_R)\,\theta'^2\theta'^* + c_F\left(\frac{\overline{A'}}{b'} + \frac{\tilde{A}'}{b'}\cos\Omega t'\right)\theta'^* + (1+\mathrm{i})\,\delta c_L\theta' + \mathrm{i}c_Q|\theta'|\theta'. \tag{1.3}$$

Owing to the time dependence of a coefficient, the above dynamical system is

† Present address: DITS, University of Rome 'La Sapienza', Italy.
‡ Present address: Department of Mechanical Engineering, Technion, Haifa, Israel.

non–autonomous: complicated bifurcations such as period-doubling and chaos are expected as the properties of the incident waves are varied. In this Part we wish to examine such bifurcations and describe comprehensive experiments in a wave basin for a battery of gates, with the dual objectives of illustrating the nonlinear dynamics of a novel project in coastal engineering, and revealing the rich physics embodied by the Landau–Stuart equation.

To simplify subsequent analysis of (1.3) we retain the normalization used in Part 1, except that the amplitude $\overline{A'}$ of the steady part of the incident wave is used as a scale below:

$$\left.\begin{aligned} \alpha &= \frac{c_R}{c_N}, \qquad \beta = \frac{c_L}{c_F\,\overline{A'}/b'}, \qquad \gamma = \frac{c_Q}{\left(c_N\,c_F\,\overline{A'}/b'\right)^{1/2}}, \\ W &= \frac{\Delta\omega/\omega_0}{c_F\,\overline{A'}/b'}, \qquad \vartheta = \left(\frac{c_N}{c_F}\right)^{1/2} \frac{\theta'}{\left(\overline{A'}/b'\right)^{1/2}}, \qquad T = c_F\,\frac{\overline{A'}}{b'}\,\omega_0 t'. \end{aligned}\right\} \tag{1.4}$$

The evolution equation becomes

$$-\mathrm{i}\vartheta_T = W\vartheta + (1+\mathrm{i}\alpha)\,\vartheta^2\vartheta^* + (1+a\cos\sigma T)\,\vartheta^* + (1+\mathrm{i})\,\beta\vartheta + \mathrm{i}\gamma|\vartheta|\vartheta. \tag{1.5}$$

As before α represents the normalized damping due to radiation, β and γ the normalized linear and quadratic viscous damping respectively, and W represents the normalized detuning, while the normalized angular displacement ϑ is essentially the ratio between the angular displacement θ' and the square root of the incident wave amplitude divided by the modal half-period, $\left(\overline{A'}/b'\right)^{1/2}$. As new bifurcation parameters, a and σ are respectively the normalized amplitude and frequency of modulation of the incident wave

$$a = \frac{\tilde{A}'}{\overline{A'}}, \qquad \sigma = \frac{\Omega}{\omega_0 c_F \overline{A'}/b'}. \tag{1.6}$$

They will also be referred to as the forcing amplitude and frequency, respectively, of the dynamical system (1.5).

2. The non-autonomous dynamical system

With the introduction of action-angle coordinates R and ψ via $\vartheta = \mathrm{i}R^{1/2}\mathrm{e}^{\mathrm{i}\psi}$, the complex equation (1.5) can be expressed as a real, non-autonomous dynamical system

$$\left.\begin{aligned} R_T &= -2R\left[\alpha R + (1+a\cos\sigma T)\sin 2\psi + \beta + \gamma R^{1/2}\right] = -H_\psi - G_R, \\ \psi_T &= W + \beta + R - (1+a\cos\sigma T)\cos 2\psi = H_R - G_\psi. \end{aligned}\right\} \tag{2.1}$$

Here H denotes the Hamiltonian function

$$H(R,\psi,T) = \tfrac{1}{2}R^2 + R\,(W+\beta) - R\,(1+a\cos\sigma T)\cos 2\psi, \tag{2.2}$$

while G denotes the gradient function

$$G(R,\psi) = \tfrac{2}{3}\alpha R^3 + \beta R^2 + \tfrac{4}{5}\gamma R^{5/2}. \tag{2.3}$$

Later, the numerical results for ϑ can be more conveniently displayed in Cartesian

coordinates, $\vartheta = X + iY$, in terms of which (1.5) takes the following form:

$$\left.\begin{aligned} X_T &= (1 + a\cos\sigma T - W - \beta)\, Y - \beta X - (Y + \alpha X)\left(X^2 + Y^2\right) - X\left(X^2 + Y^2\right)^{1/2} \\ &= -H_Y - G_X, \\ Y_T &= (1 + a\cos\sigma T + W + \beta)\, X - \beta Y + (X - \alpha Y)\left(X^2 + Y^2\right) - \gamma Y\left(X^2 + Y^2\right)^{1/2} \\ &= H_X - G_Y. \end{aligned}\right\} \tag{2.4}$$

The Hamiltonian function H is now

$$H(X, Y, T) = \tfrac{1}{2}\left(X^2 - Y^2\right)(1 + a\cos\sigma T) + \tfrac{1}{2}(W + \beta)\left(X^2 + Y^2\right) + \tfrac{1}{4}\left(X^2 + Y^2\right)^2, \tag{2.5}$$

while the gradient function $G(X, Y)$ is

$$G(X, Y) = \tfrac{1}{2}\alpha\left(X^2 + Y^2\right)^2 + \tfrac{1}{2}\beta\left(X^2 + Y^2\right) + \tfrac{1}{3}\gamma\left(X^2 + Y^2\right)^{3/2}. \tag{2.6}$$

Note that the viscous boundary layer effects enter the conservative part as a frequency shift through the combination $W + \beta$.

Both for gaining analytical insight on the complex behaviour of the above system (2.1) or (2.4), and for comparison with the laboratory experiments where damping of all varieties is small, we first give approximate local and global analyses for small coefficients α, β, γ and low modulational amplitude a. The results will be used to check and to guide the more general numerical integration as well as laboratory experiments.

3. The mathematical limit of zero damping and forcing

Setting to zero the forcing amplitude a and all the damping coefficients (radiation, linear and quadratic) in (2.1), the reduced dynamical system in action-angle form is

$$R_T = -2R\sin 2\psi, \quad \psi_T = W + R - \cos 2\psi. \tag{3.1}$$

There are at most three fixed points: one at the origin and two elsewhere,

$$\mathrm{O} = \left\{0, \tfrac{1}{2}\cos^{-1} W\right\}, \qquad \mathrm{s} = \{1 - W, 0\}, \qquad \mathrm{u} = \left\{-1 - W, \tfrac{\pi}{2}\right\}. \tag{3.2}$$

The Jacobian of the linearized system is

$$\boldsymbol{J}(R, \psi) = \begin{bmatrix} -2\sin 2\psi & -4R\cos 2\psi \\ 1 & 2\sin 2\psi \end{bmatrix}. \tag{3.3}$$

It follows easily that the origin is an unstable saddle if $|W| < 1$, and a centre with oscillation frequency $\lambda = 2\left(W^2 - 1\right)^{1/2}$ if $|W| > 1$. The fixed point s exists only if $W < 1$ and is a centre with oscillation frequency $\lambda = 2(1 - W)^{1/2}$. The fixed point u exists if $W < -1$ and is an unstable saddle. Sample phase trajectories obtained by plotting the contours of constant Hamiltonian are shown in figure 1(a, b, c) for $W = 1.5$, $W = 0$ and $W = -1.5$ respectively.

As an alternative, the linearized system in Cartesian form is

$$X_T = (1 - W)\, Y - Y\left(X^2 + Y^2\right), \quad Y_T = (1 + W)\, X + X\left(X^2 + Y^2\right). \tag{3.4}$$

There are at most five, instead of three, fixed points located at

$$\mathrm{O} = \{0, 0\}, \quad \begin{Bmatrix} \mathrm{s}_1 \\ \mathrm{s}_2 \end{Bmatrix} = \left\{0, \pm(1 - W)^{1/2}\right\}, \quad \begin{Bmatrix} \mathrm{u}_1 \\ \mathrm{u}_2 \end{Bmatrix} = \left\{\pm(-1 - W)^{1/2}, 0\right\}. \tag{3.5}$$

Denoting

$$R_s = 1 - W, \quad \psi_s = 0, \tag{3.6}$$

the fixed point s is related to $s_{1,2}$ of (3.5) by

$$\begin{Bmatrix} X_{s_1} \\ X_{s_2} \end{Bmatrix} = \mp {R_s}^{1/2} \sin \psi_s, \qquad \begin{Bmatrix} Y_{s_1} \\ Y_{s_2} \end{Bmatrix} = \pm {R_s}^{1/2} \cos \psi_s. \tag{3.7}$$

Similarly, by denoting

$$R_u = -1 - W, \quad \psi_u = \pi/2 \tag{3.8}$$

u is related to $u_{1,2}$ by

$$\begin{Bmatrix} X_{u_1} \\ X_{u_2} \end{Bmatrix} = \mp {R_u}^{1/2} \sin \psi_u, \qquad \begin{Bmatrix} Y_{u_1} \\ Y_{u_2} \end{Bmatrix} = \pm {R_u}^{1/2} \cos \psi_u. \tag{3.9}$$

Phase portraits equivalent to figure 1(a, b, c) are shown in figure 1(d, e, f).

For weak oscillations around s or $s_{1,2}$ the effects of weak dissipation and forcing can be easily analysed for the simplest case where the modulational frequency of the incident waves σ is not equal to any rational multiples of $\lambda = 2(1 - W)^{1/2} \equiv 2{R_s}^{1/2}$. The gate envelope θ then responds linearly without resonance and oscillates at the same modulational frequency. The synchronous modulational response has been recently brought to the attention both theoretically and experimentally by Jiang *et al.* (1996) in the context of Faraday waves. By straightforward perturbation analysis (for $a \ll 1$ and $\alpha, \beta, \gamma = O\left(a^2\right)$) it can be shown that the natural oscillation must damp out in time, and, in action-angle form, the forced oscillation is given to the leading order by

$$R = R_s - \frac{a\lambda^2}{\sigma^2 - \lambda^2} \cos \sigma T + O(a^2), \qquad \psi = \frac{a\sigma}{\sigma^2 - \lambda^2} \sin \sigma T + O(a^2). \tag{3.10}$$

Thus the envelope of the gates responds without resonance and synchronously to the incident wave modulation. Equation (3.10) of course becomes singular as $\sigma \to \lambda$, corresponding to synchronous modulational resonance. The perturbation analysis also reveals other possibilities of subharmonic and superharmonic resonances. In the next section these resonances will be analysed asymptotically by the method of multiple scales, as in Trulsen & Mei (1995).

4. Local bifurcations of the gate envelope

Because of the myriad frequencies involved, it is important to stress that σ is the normalized frequency of the wave envelope and λ is the normalized natural frequency of the gate envelope. Recall that the incident wave has the carrier frequency $2(\omega_0 + \Delta\omega)$), and the gate oscillates at the central frequency $\omega_0 + \Delta\omega$. In this section we shall focus on the effects of a slight detuning of the wave envelope modulation from the gate envelope oscillation, i.e. the difference between $m\sigma$ and $n\lambda$, with m, n being integers. This modulational detuning should be distinguished from W, which is the normalized detuning $\Delta\omega$ of the carrier wave from the natural frequency ω_0 of the trapped mode (cf. (1.4)).

4.1. *Subharmonic modulational resonance*

Let μ be a small ordering parameter; the frequency detuning of the incident wave envelope as well as the modulation amplitude and damping also are small, i.e.

$$\sigma = 2\left(\lambda + \mu^2 d_2\right), \quad a = \mu^2 a_2, \quad \alpha = \mu^2 \alpha_2, \quad \beta = \mu^2 \beta_2, \quad \gamma = \mu^2 \gamma_2. \tag{4.1}$$

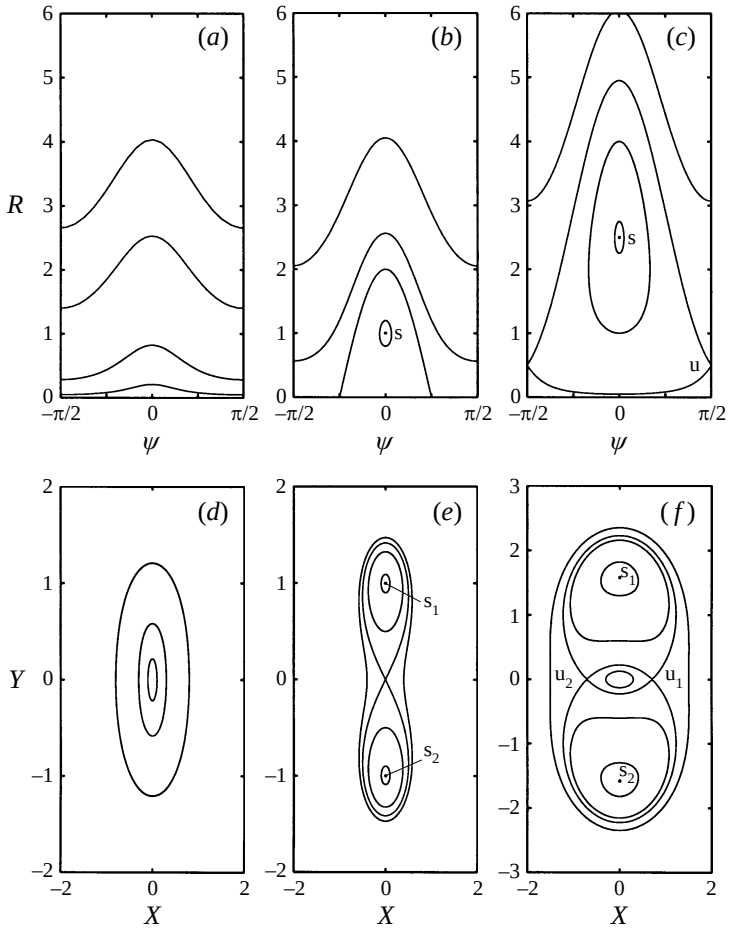

FIGURE 1. Sample phase planes for limiting Hamiltonian system. (a, b, c) Phase planes in action-angle coordinates. Trajectories flow from left to right. (a) $W = 1.5$; (b) $W = 0$; (c) $W = -1.5$. (d, e, f) Phase planes in Cartesian coordinates. Trajectories flow counterclockwise. (d) $W = 1.5$; (e) $W = 0$; (f) $W = -1.5$.

We Taylor expand system (2.1) about the non-trivial fixed point s, $R = R_s \equiv 1 - W$, $\psi = \psi_s \equiv 0$, and introduce the new slow time scale $T_2 = \mu^2 T$ and the multiple-scale expansions

$$R = R_s + \sum_{p=1}^{3} \mu^p R_p + O(\mu^4), \qquad \psi = \sum_{p=1}^{3} \mu^p \psi_p + O(\mu^4). \tag{4.2}$$

The $O(\mu)$ system is homogeneous and corresponds to an undamped oscillator of natural frequency $\lambda = 2R_s^{1/2}$ and without forcing ($a = 0$)

$$R_{1_T} + \lambda^2 \psi_1 = 0, \quad \psi_{1_T} - R_1 = 0. \tag{4.3}$$

The response is a limit cycle and can be expressed in the form

$$R_1 = R_{11} e^{-i(\lambda + \mu^2 d_2)T} + *, \qquad \psi_1 = \psi_{11} e^{-i(\lambda + \mu^2 d_2)T} + *, \tag{4.4}$$

where $R_{11} = R_{11}(T_2), \psi_{11} = \psi_{11}(T_2)$ are undetermined at this order.

At $O(\mu^2)$, we have

$$\left.\begin{aligned} R_{2_T} + \lambda^2 \psi_2 &= -4R_1\psi_1 - \lambda^2\left(\lambda^2\alpha_2 + 4\beta_2 + 2\lambda\gamma_2\right)/8, \\ \psi_{2_T} - R_2 &= 2\psi_1^2 + \beta_2 - a_2\cos\left[2\left(\lambda + \mu^2 d_2\right)T\right]. \end{aligned}\right\} \tag{4.5}$$

Thus only the zeroth and second harmonics are forced through the quadratic terms. The second harmonic is also forced by the modulation amplitude a_2. The solution is of the form

$$R_2 = R_{20} + R_{22}\mathrm{e}^{-\mathrm{i}2\left(\lambda+\mu^2 d_2\right)T} + *, \quad \psi_2 = \psi_{20} + \psi_{22}\mathrm{e}^{-\mathrm{i}2\left(\lambda+\mu^2 d_2\right)T} + *. \tag{4.6}$$

The amplitudes of the forced harmonics (2,0) and (2,2) are easily found.

At $O(\mu^3)$, the system is

$$\left.\begin{aligned} R_{3_T} + \lambda^2\psi_3 = &-R_{1_{T_2}} - 4R_2\psi_1 - 4R_1\psi_2 - R_1\left(\lambda^2\alpha_2 + 2\beta_2 + \tfrac{3}{2}\lambda\gamma_2\right) \\ &-\lambda^2\psi_1 a_2\cos\left[2\left(\lambda + \mu^2 d_2\right)T\right], \\ \psi_{3_T} - R_3 = &-\psi_{1_{T_2}} + 4\psi_1\psi_2 - a_3\cos\left[\left(\lambda + \mu^2 d_2\right)T\right]. \end{aligned}\right\} \tag{4.7}$$

Since the problem for the first harmonic (3,1) is inhomogeneous, secular terms must be removed, yielding an evolution equation for R_{11}

$$\begin{aligned} -\mathrm{i}R_{11_{T_2}} = &\left(\frac{1}{\lambda} + \frac{12}{\lambda^3}\right)R_{11}^2 R_{11}^* + \mathrm{i}\left(\frac{\lambda^2}{2}\alpha_2 + \beta_2 + \frac{3}{4}\lambda\gamma_2\right)R_{11} \\ &+ \left(d_2 + \frac{2\beta_2}{\lambda}\right)R_{11} + \left(\frac{\lambda}{4} + \frac{1}{\lambda}\right)a_2 R_{11}^*, \end{aligned} \tag{4.8}$$

$$\psi_{11} = \frac{\mathrm{i}}{\lambda}R_{11}. \tag{4.9}$$

Equation (4.9) can be normalized to:

$$-\mathrm{i}r_{11_\tau} = r_{11}^2 r_{11}^* + \mathrm{i}Br_{11} + Dr_{11} + r_{11}^*, \tag{4.10}$$

where

$$r_{11} = \frac{R_{11}}{a_2^{1/2}}\frac{2}{\lambda}\left(\frac{\lambda^2 + 12}{\lambda^2 + 4}\right)^{1/2}. \tag{4.11}$$

The normalized effective damping coefficient is

$$B = \left(\frac{\lambda^2}{2}\alpha_2 + \beta_2 + \frac{3}{4}\lambda\gamma_2\right)\left[a_2\left(\frac{\lambda}{4} + \frac{1}{\lambda}\right)\right]^{-1}. \tag{4.12}$$

The normalized detuning is

$$D = \frac{1}{a_2}\left(d_2 + \frac{2\beta_2}{\lambda}\right)\left(\frac{\lambda}{4} + \frac{1}{\lambda}\right)^{-1}, \tag{4.13}$$

and the normalized slow time is

$$\tau = T_2 a_2\left(\frac{\lambda}{4} + \frac{1}{\lambda}\right). \tag{4.14}$$

Equation (4.10) which is also of the Landau–Stuart form governs the envelope of the limit cycle, itself the envelope of the gate oscillations. Using action-angle

variables, $r_{11} = \rho^{1/2}e^{i\phi}$, and separating real and imaginary part of (4.10), we obtain the dynamical system

$$\rho_\tau = -2\rho\,(B - \sin 2\phi)\,, \quad \phi_\tau = \rho + D + \cos 2\phi. \tag{4.15}$$

Let us begin with the trivial fixed point at the origin $\rho = 0, \cos 2\phi = -D$. Linearizing the first of (4.15) for $\rho = 0 + \rho'$, with $\rho' \ll 1$,

$$\rho'_\tau = -2B\rho' \mp \left(1 - D^2\right)^{1/2}, \tag{4.16}$$

we get

$$\rho' \propto e^{2\left[\mp\left(1-D^2\right)^{1/2} - B\right]\tau}. \tag{4.17}$$

This fixed point is unstable if

$$B < 1 \quad \text{and} \quad |D| < \left(1 - B^2\right)^{1/2}, \tag{4.18}$$

and stable otherwise. Using the definition (4.12) for B, the first condition above for instability becomes

$$a_2 > \left(\frac{\lambda^2}{2}\alpha_2 + \beta_2 + \frac{3}{4}\lambda\gamma_2\right)\left(\frac{\lambda}{4} + \frac{1}{\lambda}\right)^{-1}, \tag{4.19}$$

or in physical variables

$$\frac{\tilde{A}'}{\overline{A'}} > \left[\frac{\lambda^2}{2}\frac{c_R}{c_N} + \frac{c_L}{c_F\overline{A'}/b'} + \frac{3}{4}\lambda\frac{c_Q}{\left(c_N c_F \overline{A'}/b\right)^{1/2}}\right]\left(\frac{\lambda}{4} + \frac{1}{\lambda}\right)^{-1}. \tag{4.20}$$

Recall by definition (1.4), $\lambda = 2(1 - W)^{1/2}$ is related to detuning $\Delta\omega$ via $W = \Delta\omega b'/\omega_0 c_F \overline{A'}$.

Since $\lambda \to 0$ as $W \to 1$, the threshold for a_2 decreases to zero. In view of (1.4) for W, it follows that this subharmonic modulational resonance is easily excited by weak modulation of incident waves, when the detuning $\Delta\omega$ is positive and close to the right-hand branch TP of the region of instability shown in figure 7 of Part 1.

Using (4.12) and (4.13), the threshold of instability $|D| = \left(1 - B^2\right)^{1/2}$ corresponds to a hyperbola in the (d_2, a_2)-plane,

$$d_2 = \pm\left[a_2^2\left(\frac{\lambda}{4} + \frac{1}{\lambda}\right)^2 - \left(\frac{\lambda^2}{2}\alpha_2 + \beta_2 + \frac{3}{4}\lambda\gamma_2\right)^2\right]^{1/2} - \frac{2\beta_2}{\lambda}. \tag{4.21}$$

The region of instability lies above the hyperbola, whose vertex is located at

$$d_2 = -\frac{2\beta_2}{\lambda}, \qquad a_2 = \left(\frac{\lambda^2}{2}\alpha_2 + \beta_2 + \frac{3}{4}\lambda\gamma_2\right)\left(\frac{\lambda}{4} + \frac{1}{\lambda}\right)^{-1} \tag{4.22}$$

at which $D = 0$ and $B = 1$, marking the lowest a_2 that can destabilize the envelope.

Returning to (4.15), two other fixed points with finite amplitudes can be found as the roots of the quadratic equation

$$\rho^2 + 2D\rho + D^2 + B^2 = 1. \tag{4.23}$$

To distinguish these fixed points from s, u of the unmodulated dynamical system in Part 1, the solutions of 4.23) are denoted by

$$\mathrm{s}_m = \{\rho_s, \phi_s\}\,, \quad \mathrm{u}_m = \{\rho_u, \phi_u\}\,, \tag{4.24}$$

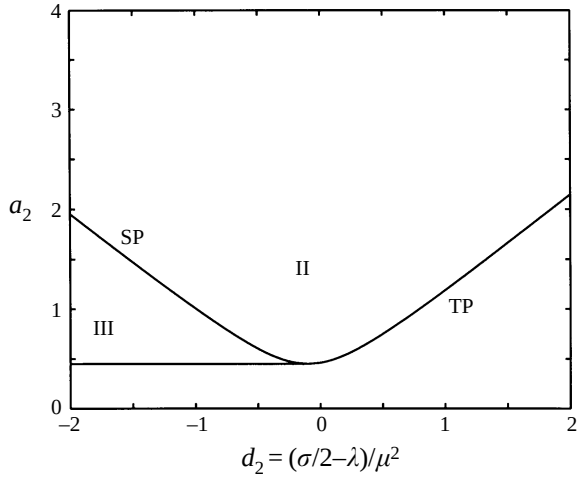

FIGURE 2. Region of instability for the subharmonic modulational resonance; $W = 0$, $\alpha_2 = \beta_2 = \gamma_2 = 0.1$, for which $B = 0.45$. Region I: stable trivial fixed point s. Region II: unstable trivial fixed point u_m coexisting with s_m (region of instability). Region III: stable trivial fixed fixed point coexisting with s_m and u_m.

where

$$\begin{Bmatrix} \rho_s \\ \rho_u \end{Bmatrix} = -D \pm \left(1 - B^2\right)^{1/2}, \tag{4.25}$$

and

$$\begin{Bmatrix} \phi_s \\ \phi_u \end{Bmatrix} = \begin{Bmatrix} 0 \\ \pi/2 \end{Bmatrix} \pm \tfrac{1}{2} \sin^{-1} B. \tag{4.26}$$

The roots (4.25) are real if $B < 1$. Since $\rho > 0$ it is necessary that $D < \left(1 - B^2\right)^{1/2}$ for s_m to exist, and $D < -\left(1 - B^2\right)^{1/2}$ for u_m to exist.

The Jacobian of the system evaluated at the fixed points (s_m, u_m) is

$$\boldsymbol{J} = \begin{bmatrix} 0 & -4\rho(\rho + D) \\ 1 & -2B \end{bmatrix}, \tag{4.27}$$

where ρ indicates either ρ_s or ρ_u. The eigenvalues are

$$-B \pm \left[B^2 - 4\rho(D + \rho)\right]^{1/2}. \tag{4.28}$$

and the larger eigenvalue is positive when

$$\rho > -D. \tag{4.29}$$

Therefore, comparing (4.29) with (4.25), it is immediately clear that s_m is always stable and u_m is always unstable.

In figure 2 a sample region of modulational instability is shown for $\alpha_2 = \beta_2 = \gamma_2 = 0.1$ and $\lambda = 2$ ($W = 0$). Along the + branch of (4.21), denoted by TP in figure 2, the origin loses stability in a transcritical pitchfork bifurcation; along the − branch, denoted by SP, the origin loses stability in a subcritical pitchfork bifurcation and the non-trivial response jumps to a finite value. Whenever the detuning d_2 and amplitude a_2 of the modulation fall above the hyperbola (region II in figure 2), the subharmonic limit cycle envelope s_m occurs. To the left of SP and above the vertex of the hyperbola

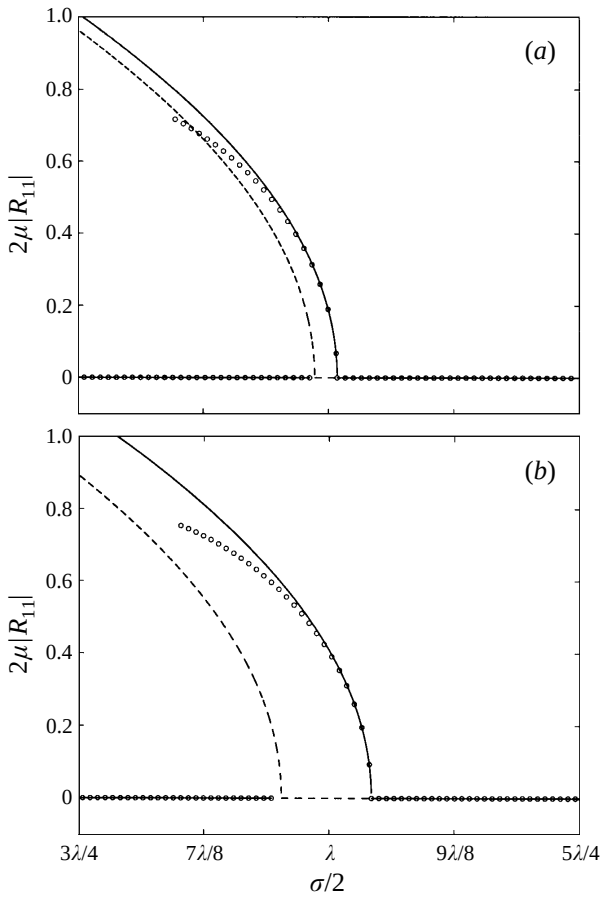

FIGURE 3. Bifurcation diagrams for $\alpha = \beta = \gamma = 0.01$ and $W = 0$. Solid and dashed lines denote the stable and the unstable analytical solutions respectively; open circles the numerical solution. (*a*) $a = 0.05$; (*b*) $a = 0.10$.

(region III in figure 2) the stable non-trivial solution s_m coexists with the unstable u_m and the stable trivial fixed point.

Now let us examine the effects of detuning W of the carrier wave. It follows from (4.21) that as $\lambda \to 0$ (i.e. as $W \to 1$) the region of instability becomes the whole half–plane $a_2 > 0$. At the same time the response decreases to zero, as can be deduced from (4.12), (4.13) and the explicit expression for the non-trivial root $\rho_s = -D + \left(1 - B^2\right)^{1/2}$. From (1.4), the condition $W \to 1$ implies that the carrier wave amplitude $\overline{A'}$ and detuning $\Delta\omega$ fall near the right branch TP of the threshold of instability in figure 7 of Part 1. Thus, although this modulational resonance can be excited more easily, the excited response must be very small in magnitude.

Sample bifurcation diagrams of modulational instability are shown for $W = 0$ and $\alpha = \beta = \gamma = 0.01$ in figure 3(*a*, *b*). The approximate predictions of the amplitude of the first harmonic $2\mu|R_{11}|$ (solid lines) are confirmed by the result of numerical integration of (1.5) (circles) for $a = 0.05$ (figure 3*a*) and $a = 0.10$ (figure 3*b*), the resonance threshold being $a = 0.045$.

4.2. *Synchronous modulational resonance*

To excite this resonance, let the modulation detuning and damping terms be $O(\mu^2)$ and the modulation amplitude even smaller:

$$\sigma = \lambda + \mu^2 d_2, \quad \alpha = \mu^2 \alpha_2, \quad \beta = \mu^2 \beta_2, \quad \gamma = \mu^2 \gamma_2, \quad a = \mu^3 a_3. \tag{4.30}$$

Expanding as in (4.2) we find the $O(\mu)$ system is again the free oscillator, so the response is of the form (4.4). Pursuing the perturbation analysis to $O(\mu^3)$ as in the last section, we find by removing the secularity for (3,1) an evolution equation for R_{11} of the Landau–Stuart type

$$-\mathrm{i}R_{11_{T_2}} = \left(\frac{1}{\lambda} + \frac{12}{\lambda^3}\right) R_{11}^2 R_{11}^* + \mathrm{i}\left(\frac{\lambda^2}{2}\alpha_2 + \beta_2 + \frac{3}{4}\lambda\gamma_2\right) R_{11} + \left(d_2 + \frac{2\beta_2}{\lambda}\right) R_{11} + \frac{\lambda}{4} a_3, \tag{4.31}$$

$$\psi_{11} = \frac{\mathrm{i}}{\lambda} R_{11}. \tag{4.32}$$

Equation (4.32) differs from (4.9) only in the forcing term. Fixed points of the above equation are the amplitudes of the limit cycle around s. Straightforward analysis similar to that for subharmonic resonance shows that there can be one (stable) or three fixed points (two stable and one unstable), depending on the detuning d_2. Because of the triple-valued region, hysteresis and jump phenomena are possible. The bifurcation diagram is typical of other synchronous resonance of nonlinear systems, similar to the Duffing problem with a soft spring (see for example Jordan & Smith 1987). Details are omitted here (see Sammarco 1996).

We have also carried out a similar asymptotic analysis for the superharmonic modulational resonance where the modulational frequency is $\sigma = \left(\lambda + \mu^2 d_2\right)/2$ (Sammarco 1996).

As is well known for dissipative systems, period-doubling by subharmonic resonance can be a prelude to chaos and strange attractors. This will be examined numerically in a later section.

5. Global bifurcations

Recall in figure 1 that in the Hamiltonian limit there is a saddle point for $|W| < 1$ and two saddle points for $W < -1$. With additional higher-order terms the homoclinic or heteroclinic orbits through the saddles may be disturbed to yield horseshoe tangles and to provide the lower bound for global chaos. For the onset of these global bifurcations we employ the Melnikov method (Guckenheimer & Holmes 1983) which applies to a slightly perturbed system of the form

$$R_T = f_1(R, \psi) + \mu g_1(R, \psi, T), \quad \psi_T = f_2(R, \psi) + \mu g_2(R, \psi, T), \tag{5.1}$$

with f_1, f_2 being Hamiltonian, g_1, g_2 periodic in T, and $\mu \ll 1$. Let the homoclinic orbit of the associated Poincaré map of the Hamiltonian part be denoted by $\left\{R^h(T), \psi^h(T)\right\}$. Then the zero of the Melnikov function

$$M = \int_{-\infty}^{\infty} \mathrm{d}T \ \left[f_1(R^h, \psi^h) g_2(R^h, \psi^h, T) - f_2(R^h, \psi^h) g_1(R^h, \psi^h, T)\right] \tag{5.2}$$

gives approximately the threshold for Smale's horseshoe which is a prelude to global chaos. We now assume that all dampings and modulational forcing are $O(\mu)$ which is

a small ordering parameter unrelated to μ in the last section:

$$\alpha = \mu\alpha_1, \quad \beta = \mu\beta_1, \quad \gamma = \mu\gamma_1, \qquad a = \mu a_1. \tag{5.3}$$

Then system (2.1) can be recast in the form (5.1) with

$$\left.\begin{aligned} f_1 &= -2R\sin 2\psi, \\ g_1 &= -2R\left(\alpha_1 R + \beta_1 + \gamma_1 R^{1/2} + a_1\cos\sigma T\sin 2\psi\right) \\ f_2 &= W + R - \cos 2\psi, \\ g_2 &= -\left(\beta_1 + a_1\cos\sigma T\cos 2\psi\right). \end{aligned}\right\} \tag{5.4}$$

First we analyse the homoclinic connection for $|W| < 1$, then the heteroclinic connections for $W < -1$.

5.1. *Homoclinic orbit, $|W| < 1$*

Referring to figure 1(*b*) (for $W = 0$), the homoclinic orbit $\{R^h, \psi^h\}$ is the phase curve that goes from $\{R, \psi\} = \{0, -\pi/4\}$ to $\{0, \pi/4\}$. Since the orbit passes through the origin of the phase plane, the Hamiltonian (2.2) with $a = \beta = \gamma = 0$ vanishes:

$$H(R, \psi) = H\left(0, \tfrac{1}{2}\cos^{-1} W\right) = 0, \quad \text{i.e.} \quad \tfrac{1}{2}R + W - \cos 2\psi = 0. \tag{5.5}$$

It follows from f_2 of (5.4) that

$$\psi_T^h = \cos 2\psi - W, \tag{5.6}$$

which can be integrated with the initial condition that $\psi^h(0; W) = 0$. Afterwards R^h can be obtained from (5.5), with the initial condition $R^h(0; W) = 2(1 - W)$. The results are

$$R^h(T - T_0; W) = \frac{2\left(1 - W^2\right)}{W + \cosh\left[2\kappa\left(T - T_0\right)\right]}, \tag{5.7}$$

$$\psi^h(T - T_0; W) = \arctan\left\{\left(\frac{1 - W}{1 + W}\right)^{1/2}\tanh\left[\kappa\left(T - T_0\right)\right]\right\}. \tag{5.8}$$

For brevity we have defined $\kappa = \left(1 - W^2\right)^{1/2}$.

The Melnikov function is given by

$$\begin{aligned} M(\sigma, T_0; W, \alpha_1, \beta_1, \gamma_1, a_1) &= \int_{-\infty}^{\infty} \mathrm{d}T\ \left[f_1 g_2 - f_2 g_1\right]_{R=R^h, \psi=\psi^h} \\ &= \int_{-\infty}^{\infty} \mathrm{d}T\ 2R^h\left[a_1\left(W + R^h\right)\sin 2\psi^h\cos\sigma T - \beta_1\sin 2\psi^h\right. \\ &\qquad \left. + \left(W + R^h - \cos 2\psi^h\right)\left(\alpha_1 R^h + \beta_1 + \gamma_1 R^{h\,1/2}\right)\right]. \end{aligned} \tag{5.9}$$

Substituting expressions (5.7) and (5.8) into the integrands of (5.9), we get

$$M = \Pi^{\alpha}(W)\alpha_1 + \Pi^{\beta}(W)\beta_1 + \Pi^{\gamma}(W)\gamma_1 - \Pi^{a}(\sigma, W)a_1\sin\sigma T_0 \tag{5.10}$$

where all but $\Pi^{\gamma}(W)$ can be explicitly evaluated by contour integration†

$$\begin{aligned} \Pi^{\alpha}(W) &= \int_{-\infty}^{\infty} \mathrm{d}T\ 2R^{h2}\left(W + R^h - \cos 2\psi^h\right) \\ &= 4\left[\left(1 + 2W^2\right)\left(\frac{\pi}{2} - \arctan\frac{W}{\kappa}\right) - 3W\kappa\right], \end{aligned} \tag{5.11}$$

† O. Gottlieb, 1995, in an unpublished study on edge waves.

$$\Pi^{\beta}(W) = \int_{-\infty}^{\infty} \mathrm{d}T\ 2R^h \left(W + R^h - \cos 2\psi^h - \sin 2\psi^h\right)$$
$$= 4\left[W\left(-\frac{\pi}{2} + \arctan\frac{W}{\kappa}\right) + \kappa\right], \tag{5.12}$$
$$\Pi^{\gamma}(W) = \int_{-\infty}^{\infty} \mathrm{d}T\ 2R^{h^{3/2}} \left(W + R^h - \cos 2\psi^h\right)$$
$$= \left(2^{1/2}\kappa\right)^5 \int_{-\infty}^{\infty} \mathrm{d}T\ \{W + \cosh\left[2\kappa\left(T - T_0\right)\right]\}^{-5/2}, \tag{5.13}$$
$$-\Pi^{a}(\sigma, W) \quad \sin\sigma T_0 = \int_{-\infty}^{\infty} \mathrm{d}T\ 2R^h \left(W + R^h\right) \sin 2\psi^h \cos\sigma T$$
$$= -\pi\sigma^2 \sin\sigma T_0\ \cosh\left(\frac{\sigma \arccos W}{2\kappa}\right) \Big/ \sinh\left(\frac{\pi\sigma}{2\kappa}\right). \tag{5.14}$$

Π^{γ} can only be evaluated numerically. Details can be found in Sammarco (1996).

For fixed $\alpha_1, \beta_1, \gamma_1, W, \sigma$, the Melinkov function (5.10) oscillates sinusoidally with T_0. Therefore the necessary condition $M = 0$ is met when

$$a_1 = \frac{\Pi^{\alpha}(W)\ \alpha_1 + \Pi^{\beta}(W)\ \beta_1 + \Pi^{\gamma}(W)\ \gamma_1}{\Pi^{a}(\sigma, W)}. \tag{5.15}$$

For fixed damping constants, homoclinic tangle occurs when the forcing amplitude a_1 exceeds the above value. Equation (5.15) is linear in $\alpha_1, \beta_1, \gamma_1$. Therefore, for fixed W and σ, the smaller the dissipation coefficients, the lower the threshold for forcing a_1 to give rise to horseshoe tangles.

On the other hand, for given values of the dissipation coefficients, (5.15) has a nonlinear dependence on both the detuning of the carrier wave W and on the frequency of modulation σ. Figure 4 shows the dependence of the threshold on σ for $W = -0.99, 0, 0.9$. First, the coefficients of the three damping coefficients α_1, β_1, γ_1,

$$\frac{\Pi^{\alpha}(W)}{\Pi^{a}(\sigma, W)}, \qquad \frac{\Pi^{\beta}(W)}{\Pi^{a}(\sigma, W)}, \qquad \frac{\Pi^{\gamma}(W)}{\Pi^{a}(\sigma, W)}, \tag{5.16}$$

are shown in figure 4(a, b, c). Then in figure 4(d) the threshold (5.15) is displayed for $\alpha_1 = \beta_1 = \gamma_1 = 0.1$. For different W the three ratios in (5.16) depend similarly on σ. They all have a minimum which decreases in magnitude and shifts towards lower frequency for larger W. Hence positively detuned carrier waves with low frequency of modulation can lead to homoclinic tangles even with very small a.

It can also be shown that for a given σ and varying W, the threshold a_1 has a minimum which decreases with σ, and moves towards positive W.

Let us compare the period-doubling threshold with the threshold for homoclinic tangles. Multiplying (4.21) by μ^2 we get the threshold for period doubling in terms of $\sigma = 2\left(\lambda + \mu^2 d_2\right)$ and a:

$$\sigma = 2\left\{\lambda \pm \left[a^2\left(\frac{\lambda}{4} + \frac{1}{\lambda}\right)^2 - \left(\frac{\lambda^2}{2}\alpha + \beta + \frac{3}{4}\lambda\gamma\right)^2\right]^{1/2} - \frac{2\beta}{\lambda}\right\}, \tag{5.17}$$

where $\lambda = 2\left(1 - W\right)^{1/2}$. Similarly multiplication of (5.15) by μ yields

$$a = \frac{\Pi^{\alpha}(W)\ \alpha + \Pi^{\beta}(W)\ \beta + \Pi^{\gamma}(W)\ \gamma}{\Pi^{a}(\sigma, W)}. \tag{5.18}$$

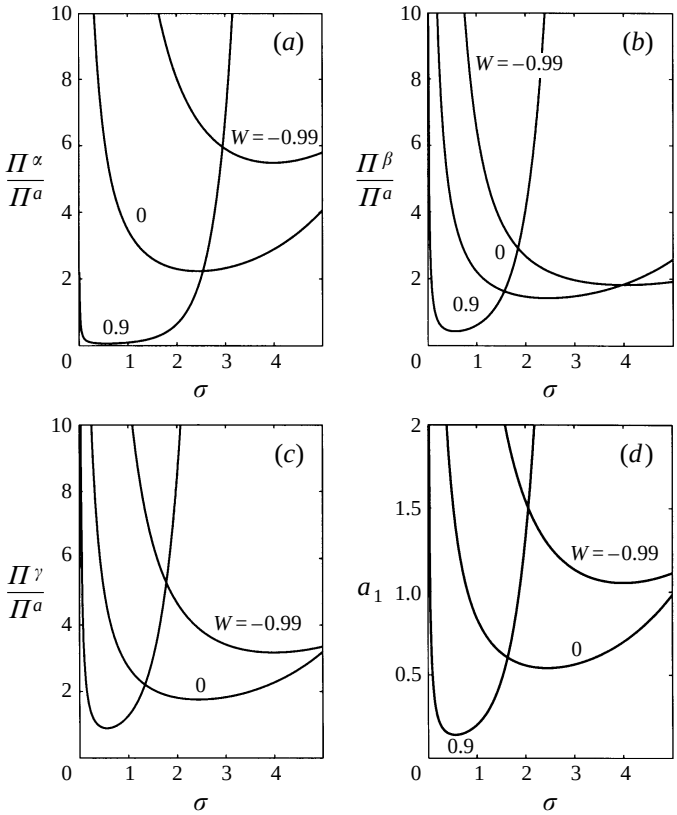

FIGURE 4. Melnikov's thresholds for homoclinic tangle. (*a*) Factor α_1 for radiation damping; (*b*) factor β_1 for linear viscous damping; (*c*) factor γ_1 for quadratic damping ; (*d*) thresholds for homoclinic tangle for $\alpha_1 = \beta_1 = \gamma_1 = 0.1$

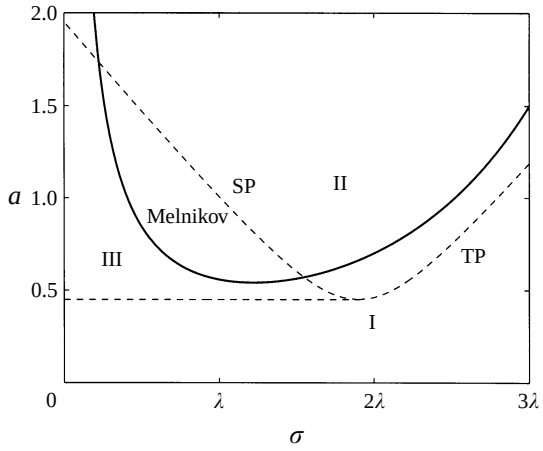

FIGURE 5. Threshold for homoclinic tangles, compared with the instability threshold for subharmonic resonance, for $W = 0$.

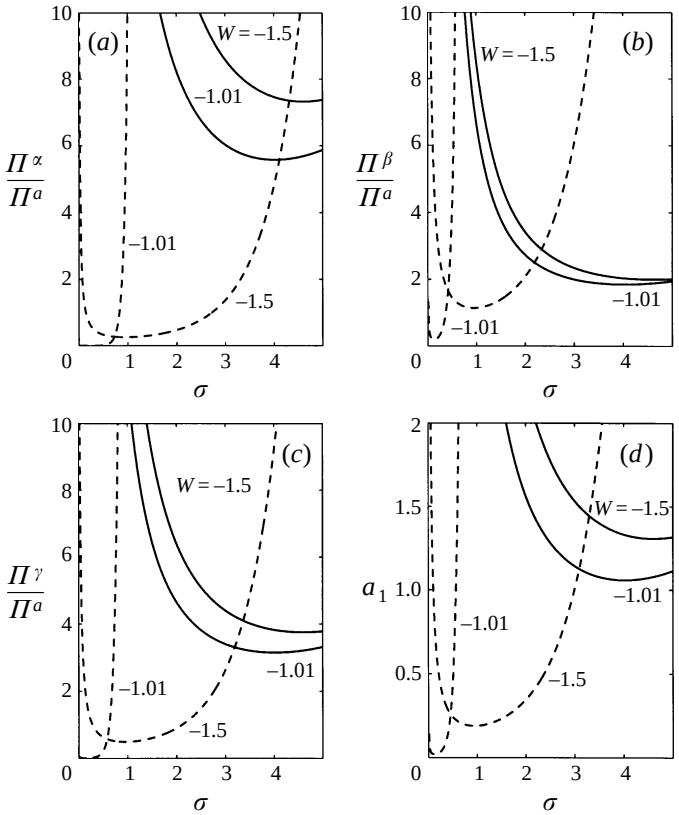

FIGURE 6. Melnikov's thresholds for heteroclinic tangle; solid lines are for the upper connection, dashed lines are lower connection. (*a*) Factor α_1 for radiation damping ; (*b*) factor β_1 for linear viscous damping ; (*c*) factor γ_1 for quadratic damping ; (*d*) thresholds for heteroclinic tangle for $\alpha_1 = \beta_1 = \gamma_1 = 0.1$

For $\alpha = \beta = \gamma = 0.1$ and $W = 0$ the two thresholds (5.17) and (5.18) are plotted in figure 5. Above the threshold of Melnikov, a homoclinic tangle is possible. In region II period doubling occurs; in region III synchronous and period-doubled responses are both possible. Figure 5 shows that for a given modulational frequency σ, as the amplitude of the modulation a increases, period doubling precedes homoclinic tangles. It can also be seen that natural frequency of the centre λ and critical frequency for a homoclinic tangle are of comparable magnitude.

5.2. *Heteroclinic orbits, $W < -1$*

When $W < -1$, heteroclinic orbits are the phase curves connecting $\{R, \psi\} = \{-1 - W, -\pi/2\}$ and $\{-1 - W, \pi/2\}$ above and below the centre s. They have been illustrated for $W = -1.5$ in figure 1(*c*).

The two heteroclinic connections for $W < -1$ correspond to a constant Hamiltonian with

$$H(R, \psi) = H(-1 - W, \mp\pi/2) \equiv -\tfrac{1}{2}(1 + W)^2. \tag{5.19}$$

Using (2.2) for the Hamiltonian with $a = 0$ and solving for R gives

$$R = -W + \cos 2\psi \pm [(1 + \cos 2\psi)(-1 - 2W + \cos 2\psi)]^{1/2}. \tag{5.20}$$

Substitution in f_2 of (5.4) gives a first-order equation in ψ only:

$$\psi_T = \pm \frac{1}{2\cos\psi\left(-W-1+\cos^2\psi\right)^{1/2}}, \tag{5.21}$$

which can be integrated subject to the initial conditions at $T = T_0$, $\psi^{h\pm}(0;W) = 0$. $R^{h\pm}$ can then be obtained from (5.20). Finally, the heteroclinic orbits $R^{h\pm}, \psi^{h\pm}$ are

$$R^{h\pm}(T-T_0;W) = -(1+W)\frac{(-W)^{1/2}\cosh\left[2\kappa(T-T_0)\right]\pm 1}{(-W)^{1/2}\cosh\left[2\kappa(T-T_0)\right]\mp 1}, \tag{5.22}$$

$$\psi^{h\pm}(T-T_0;W) = \arctan\left\{\left(\frac{W}{1+W}\right)^{1/2}\sinh\left[2\kappa(T-T_0)\right]\right\}, \tag{5.23}$$

where the $\pm$ superscript refers to the upper and lower orbits and κ is the shorthand for $(-1-W)^{1/2}$; note that $R^{h\pm}$ satisfies the initial condition $R^{h\pm}(0;W) = \left[(-W)^{1/2}\pm 1\right]^2$.

Upon substitution of (5.22) (5.23) into (5.9) we obtain for each of the two orbits a Melnikov function which has the same form as (5.10), but with

$$\Pi^{\alpha\pm}(W) = \mp 4W\left[(W-2)\left(\arctan\kappa - \left\{\begin{array}{c}\pi\\0\end{array}\right\}\right)+3\kappa\right], \tag{5.24}$$

$$\Pi^{\beta\pm}(W) = \pm 4\left[W\left(\arctan\kappa - \left\{\begin{array}{c}\pi\\0\end{array}\right\}\right)+\kappa\right], \tag{5.25}$$

$$\begin{aligned}\Pi^{\gamma\pm}(W) = \pm 4(1+W)^2\left[W(1+W)\right]^{1/2}&\int_{-\infty}^{\infty} \mathrm{d}T\cosh\left[2\kappa(T-T_0)\right]\\ &\times\left\{(-W)^{1/2}\cosh\left[2\kappa(T-T_0)\right]\pm 1\right\}^{1/2}\\ &\times\left\{(-W)^{1/2}\cosh\left[2\kappa(T-T_0)\right]\mp 1\right\}^{-5/2},\end{aligned} \tag{5.26}$$

$$\Pi^{a\pm}(\sigma,W) = \pi\sigma^2\frac{\cosh\left\{\sigma\left[\arccos\left(1/(-W)^{1/2}\right)-\left\{\begin{array}{c}\pi\\0\end{array}\right\}\right]\Big/ 2\kappa\right\}}{\sinh\left(\pi\sigma/2\kappa\right)}. \tag{5.27}$$

$\Pi^{\alpha\pm}$, $\Pi^{\beta\pm}$ and $\Pi^{a\pm}$ are found analytically. $\Pi^{\gamma\pm}$ can be evaluated only numerically. Details are given in Sammarco (1996).

In figure 6(a,b,c) the three ratios of (5.16) are plotted for the lower and upper orbits respectively by dashed and solid lines. With the same line styles, figure 6(d) shows the thresholds for $\alpha_1 = \beta_1 = \gamma_1$ of the two orbits.

For each orbit the contributions from the three dissipation sources (radiation, linear and quadratic viscous) behave similarly. As the detuning frequency W decreases from -1, the thresholds increase for both the upper orbits (solid lines) and the the lower orbit (dashed line). Note that for detuning increasingly closer to -1, horseshoe tangles of the lower orbit occur practically at $a_1 = 0$ and for increasingly smaller frequency.

On the other hand the threshold for the upper orbit is very high ($a_1 > 1$). By taking the limit $W \to -1$ of expressions (5.11) to (5.14) and of $(5.24)^+$ to $(5.27)^+$ (or by simply comparing figures 4 and 6) it can be seen that as $W \to -1$ the threshold for the upper heteroclinic orbit approaches the threshold for the homoclinic orbit, in agreement with the fact that the heteroclinc orbits reduce to homoclinic orbits when $W = -1$. In the same limit, the threshold for the lower heteroclinic orbit has

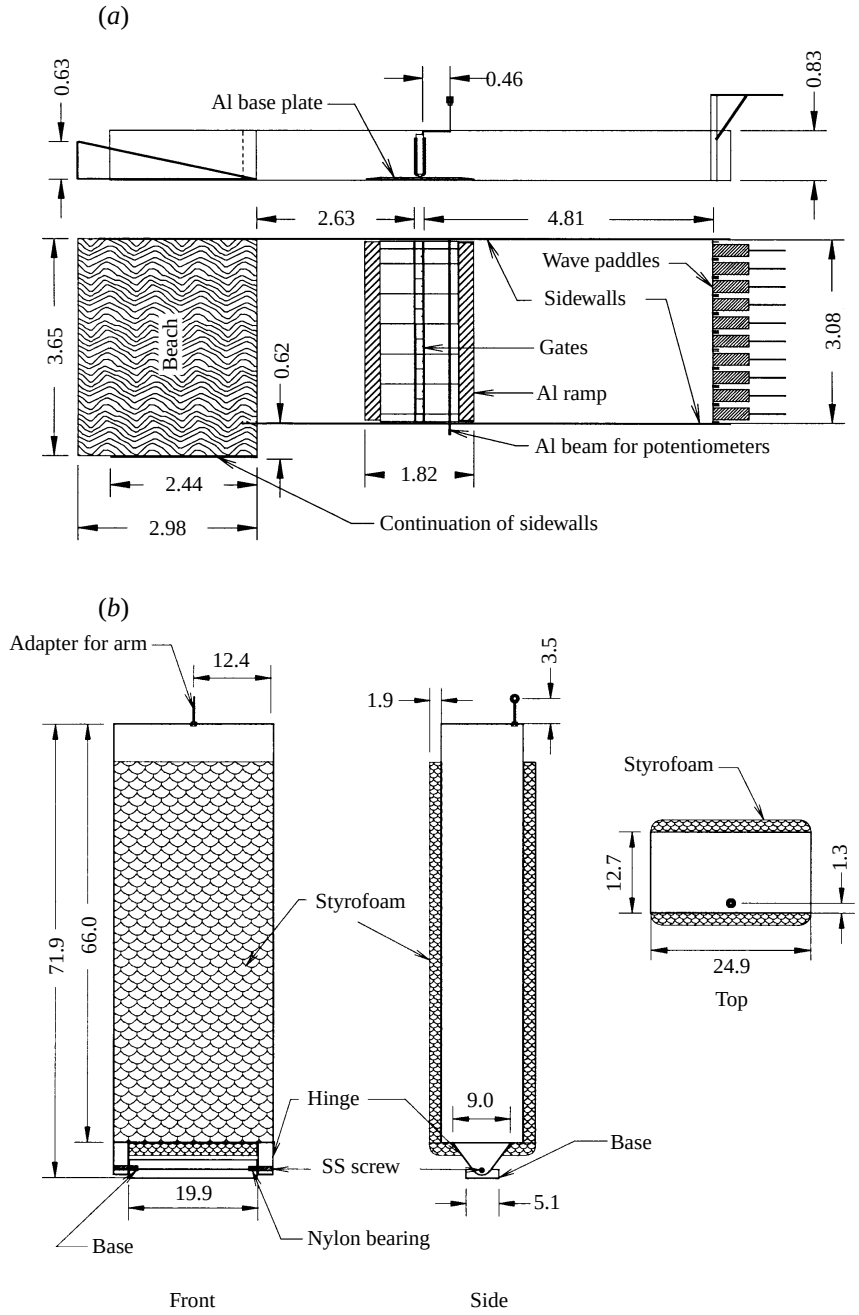

FIGURE 7. (*a*) Wave basin setup. Dimensions in m. (*b*) Model gate in the basin experiment. Dimensions in cm.

a minimum that tends to zero; however the area above the threshold curve also dimnishes to zero, i.e. both the left- and right-branches of the threshold curve tends to the line $\sigma = 0$. Thus it is the threshold of the upper heteroclinic orbit that matters.

We have performed many numerical simulations based on direct integration of (2.1) or, equivalently, (2.4). For brevity we shall only discuss results corresponding to the

laboratory experiments with a view to uncovering the various bifurcations including chaos. The experiments are therefore discussed first.

6. Laboratory observation of envelope bifurcations

6.1. *The experimental setup*

Preliminary tests for the two-gates setup in a narrow flume, as described in Part 1, failed to yield interesting results predicted by the theory, owing to the relatively large damping contributed by the sidewalls of the flume. We have therefore installed a multi-gate barrier in a wide wave basin. The gate dimensions are slightly different from those in Part 1. The general layout of the experiments is displayed in figure 7(*a*).

Thirteen hollow gates made of Plexiglas are hinged on a common horizontal axis spanning the entire width at mid-length of a wide channel, as sketched in figure 7(*b*). Two end gates next to the sidewalls are only half as wide as the other gates, in order that the sidewalls serve as two planes of mirror symmetry. The hinges are made of nylon bearings to reduce friction. Styrofoam is taped on the front and back of the gates to boost buoyancy; its edges are rounded to reduce separation losses. The water depth is maintained at 0.83 m.

Free-surface displacements are measured by four conductivity probes on the incidence side and three on the transmission side. Gate rotations are recorded by connecting potentiometers to each of the full-width gates. For this model, the eigenfrequency is $\omega_0/2\pi = 0.70$ Hz. The following coefficients of the evolution equations are computed theoretically by ignoring the rounded corners

$$c_N = 27.330,\ c_R = 2.271,\ c_F = 1.630. \tag{6.1}$$

As a preliminary step we find the frictional damping coefficients by giving neighbouring gates an equal and opposite rotation from the vertical position, and releasing them simultaneously. The time series of the free oscillations are used to determine the best damping coefficients to fit the theoretical curve, as discussed in Part 1. The results are

$$c_L = 0.01, \qquad c_Q = 0.48, \tag{6.2}$$

which are considerably less than those found in the flume with just two gates. These coefficients are used in all numerical experiments with incident waves.

6.2. *Choice of experimental parameters*

As noted in the local analysis of §4 and the global analysis of §5, period doubling and homoclinc tangles are easily excited even with low modulational amplitude a, when the carrier wave detuning is such that $W \to 1$. However in this limit the amplitude of the period-doubled limit cycle decreases to zero and becomes hard to detect experimentally. Moreover, in the same limit, $\lambda = 2(1-W)^{1/2} \to 0$. The forcing frequency σ, which must be around 2λ for a period-doubled (and eventually chaotic) response to occur, must also be small. Since small modulational frequencies correspond to long modulational periods, the neighbourhood of $W \to 1$ would demand prohibitively large data storage in experiments.

The global analysis showed that as W decreases from 1 to -1 the amplitude thresholds for the homoclinic ($|W| < 1$), and upper heteroclinic tangles ($W < -1$), become increasingly high (see figure 6); chaos is more difficult to generate experimentally. For horseshoe tangles arising from the lower heteroclinic orbit, ($W < -1$), the threshold also increases as W decreases towards -1 (cf. figure 6).

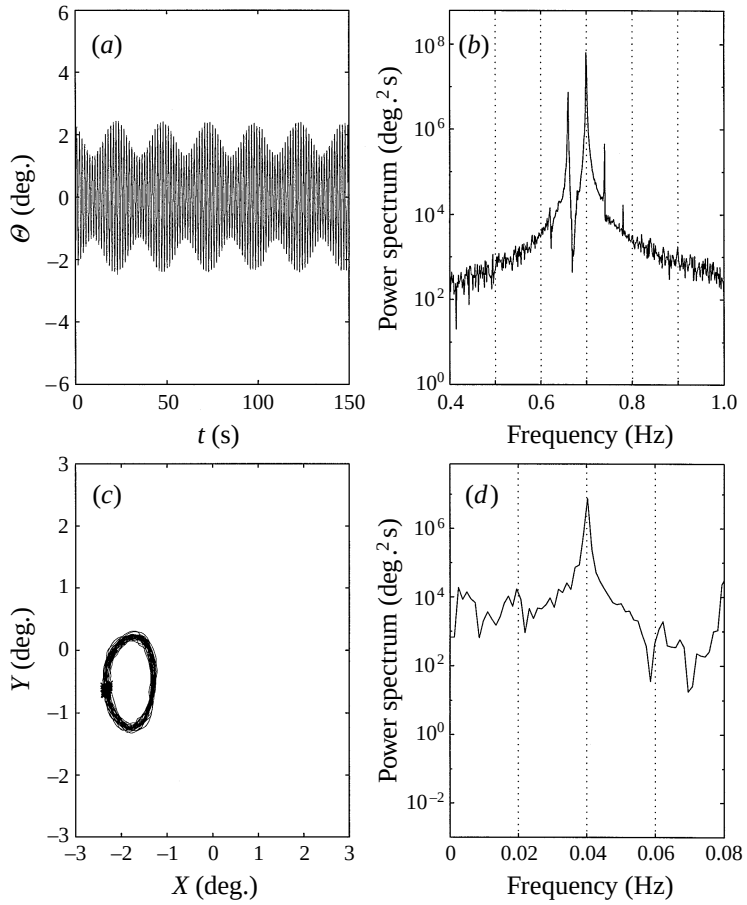

FIGURE 8. Measured gate response for $\Omega/2\pi = 0.04$ Hz, $a = 0.47$; Synchronous envelope response. (*a*) Time series of gate rotation; (*b*) spectrum of gate rotation; (*c*) envelope phase portrait and Poincaré section ; (*d*) spectrum of gate envelope.

However, in this limit, interesting dynamics occurs only for small σ, so that the need for large data storage renders the neighbourhood of $W \to -1$ also impractical for experiments.

In addition to the considerations above, cross-waves were observed on the incident side of the finite wave basin, and limit the range of frequencies that can be used to explore the bifurcation phenomenon for an infinitely long gate system. We have therefore forcused our measurements around $W = 0$. Using the values in (6.2), we find

$$\alpha = 0.0831, \qquad \beta = \frac{0.0061}{\overline{A'}/b'}, \qquad \gamma = \frac{0.0719}{\left(\overline{A'}/b'\right)^{1/2}}. \tag{6.3}$$

For an incident wave amplitude $\overline{A'} = 0.015$ m and half modal period $b' = 0.250$ m, (6.3) gives $\beta = 0.102$, $\gamma = 0.293$, i.e. $\{\alpha, \beta, \gamma\} = O(0.1)$. Thus dissipation by wave radiation and in viscous boundary layers is indeed small, while damping by vortex shedding is also not large; therefore the analytical approximations in previous sections should be relevant.

The incident wave is defined by four physical parameters: the carrier wave am-

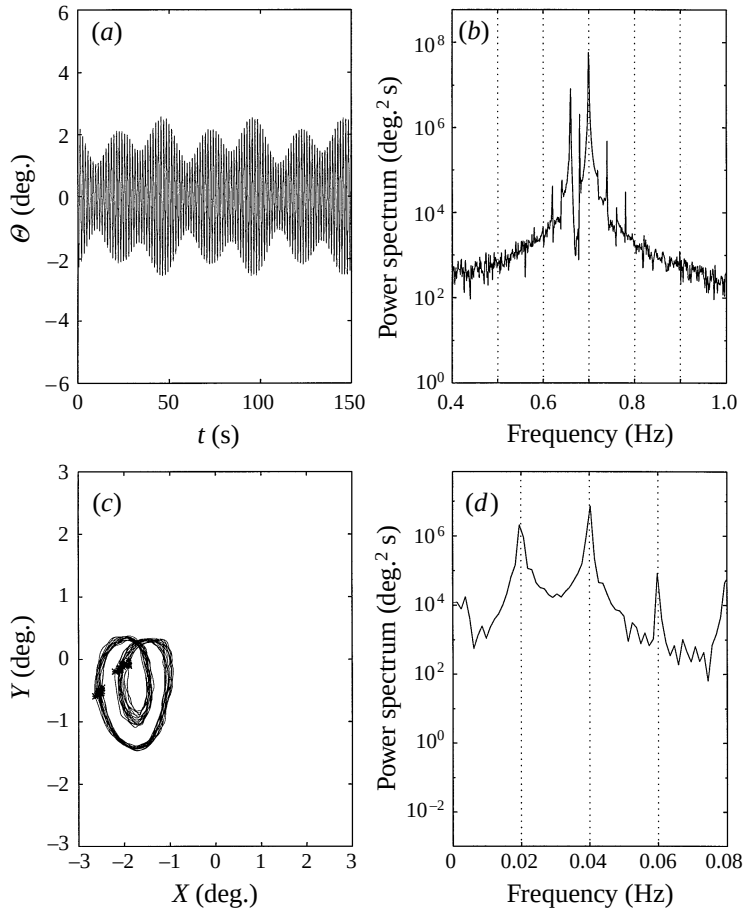

FIGURE 9. As figure 8 but for $a = 0.57$; period-two envelope response.

plitude $\overline{A}'$, the carrier wave detuning $\Delta\omega$, the modulation amplitude $\tilde{A}'$ and the modulational frequency Ω. For each carrier wave amplitude $\overline{A'}$ and detuning $\Delta\omega$, we shall seek a region in the parameter plane $(\Omega, \tilde{A}')$ for which a large variety of modulational responses (synchronous, period-doubled, chaotic) occurs within the physical constraint of the experiments.

From §4.1, the condition for subharmonic envelope bifurcation $\sigma = 2\lambda = 4(1 - W)^{1/2}$ can be recast as

$$\frac{\Omega/\omega_0}{c_F\overline{A}'/b'} = 4\left(1 - \frac{\Delta\omega/\omega_0}{c_F\overline{A}'/b'}\right)^{1/2} \quad \text{or} \quad \frac{\Delta\omega}{\omega_0} = c_F\frac{\overline{A'}}{b'} - \frac{\Omega^2}{16\omega_0^2}\frac{b'}{c_F\overline{A'}}, \tag{6.4}$$

which relates the modulational frequency Ω, the amplitude $\overline{A}'$ and detuning $\Delta\omega$ of the carrier wave.

A second condition for subharmonic modulational resonance is that the amplitude of modulation $a = \tilde{A}'/\overline{A'}$ should be larger than the threshold given by the right-hand side of (4.20). These two criteria define the regions of interest and provide guidance for the experiments.

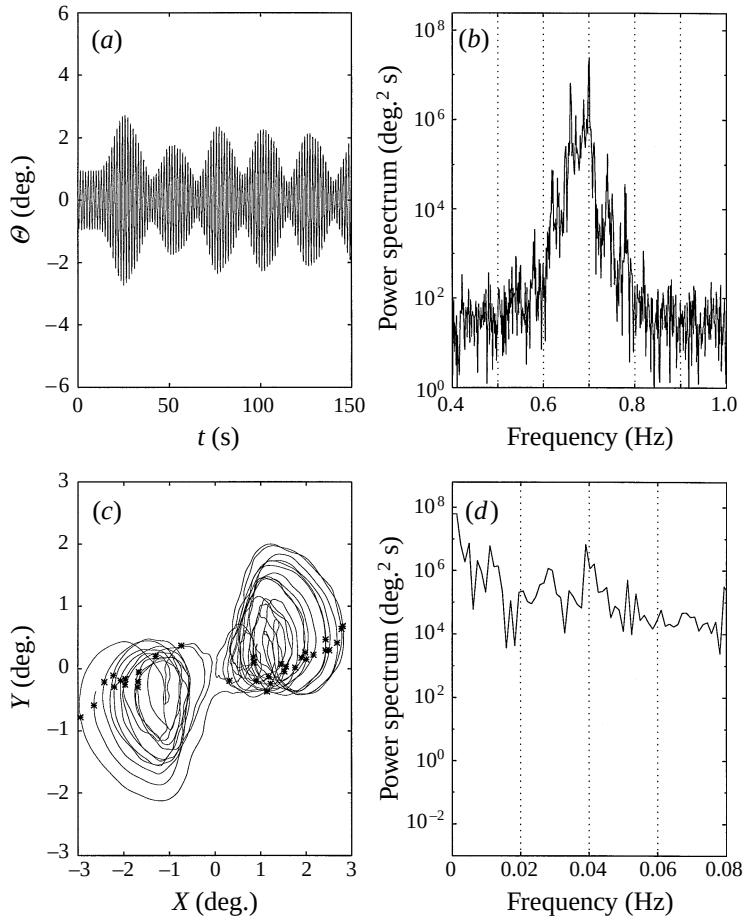

FIGURE 10. As figure 8 but for $a = 0.87$; chaotic envelope oscillations.

6.3. *Procedure of observation*

With the help of an automated system for wave generation and data acquisition, records are taken for a wide range of incident waves. As in Part 1, the amplitudes of the incident and reflected carrier waves, and the corresponding sidebands are determined from their peaks in the Fourier spectra of the free-surface displacements measured at two points x and $x + d$ on the incidence side.

The time series of the gate rotation contains information regarding the fast oscillations of the trapped mode and the slow oscillations of the envelope modulation. By the technique of Hilbert transform (Melville 1983), the time series of the envelope is extracted.

For $W = 0$, we collected data by scanning over a significant range of both Ω and a. The variety of observed bifurcation scenarios crudely resembles the numerical simulations. Here we focus attention on the details of observed data for one modulational frequency only, $\Omega/2\pi = 0.04$ Hz; this choice was made because the threshold of bifurcation is the lowest, as will be shown later. The steady component of the incident wave amplitude is fixed at $\overline{A} = 0.015$ m.

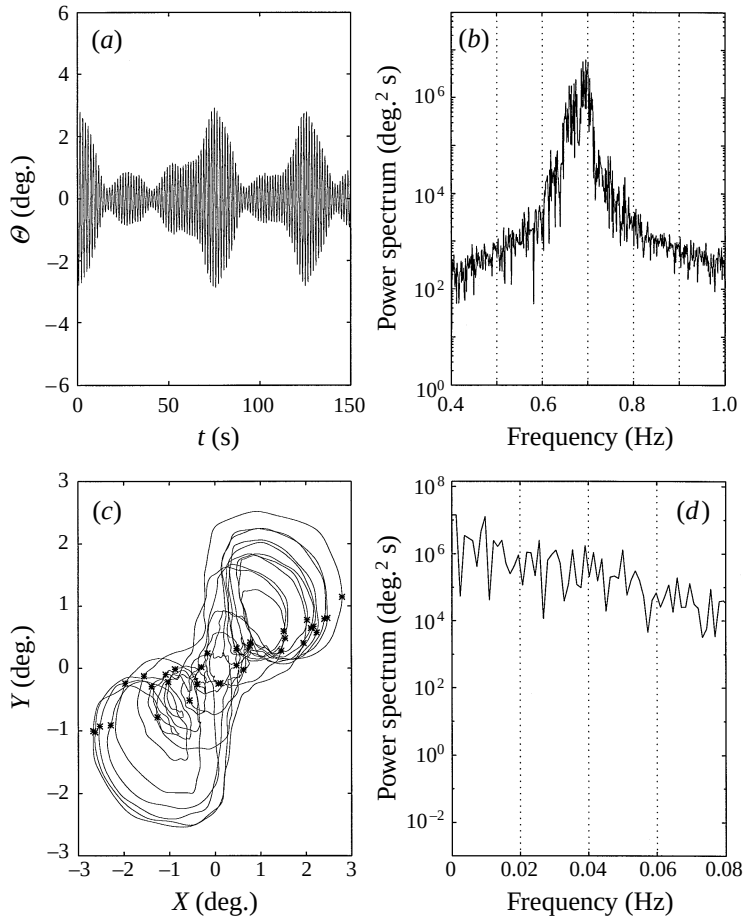

FIGURE 11. As figure 8 but for $a = 1.02$; chaotic envelope oscillations.

6.4. *Observed bifurcation scenarios*

Figure 8 shows the measured results for $a = 0.47$. Note that the left sideband is larger than the right sideband. We also remark that the inclination of the line joining the origin and the centre of the limit cycle (and the point Poincaré map of the phase curve) with respect to the X-axis depends on the choice of the initial point in the measured time series. It can be shown (Tran 1996) that as the initial point is changed along a measured time series, this line rotates around the origin of the phase plane. The size of the attractors and their distance from the origin and the envelope spectra are however unaffected, hence the rotation is inconsequential dynamically. Physically the distance between the centre of the limit cycle and the origin is the mean oscillation amplitude of the time series and measures the energy peak at half the carrier wave frequency, i.e. at $\omega_0/2\pi = 0.7$ rad s^{-1}. The size of the limit cycle is a measure of the modulation from the mean. We have also found that the phase portraits are affected strongly by the precise value of the spectral peak. The resolution of the Fourier spectrum however depends on the sampling rates. A minute shift of the peak value (by, say, 10^{-7} Hz) can make a single line appear as a thick band We therefore choose

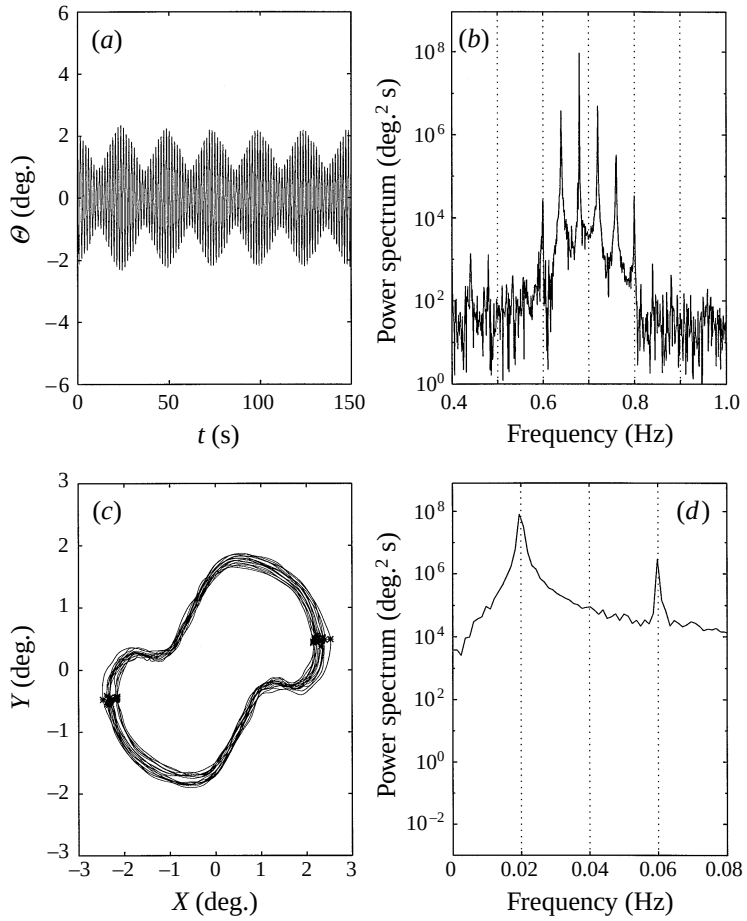

FIGURE 12. As figure 8 but for $a = 1.03$; frequency down-shift.

the peak frequency by minimizing the size of the Poincaré map which should be a point in principle.

Next, for a larger amplitude, $a = 0.57$ (figure 9), a period-two modulational response appears. The asymmetry of the sidebands is again evident.

Around $a = 0.77$ transition to chaotic oscillations is observed. Figures 10 and 11 show the observed results for $a = 0.87$ and 1.02 which are representative of the regime of the strange attractor. A period-four bifurcation from the period-doubled orbit has been identified in two cases, $a = 0.68$ and $a = 0.81$, only by a small peak at $\Omega/4$. Poincaré sections constructed from the measurements are however not sufficiently clear and are omitted.

Finally for a large amplitude of modulation, $a = 1.03$, a frequency downshift is evident, as in figure 12. The spectrum of the envelope in figure 12(*d*) has a dominant peak at $\Omega/2$ and no energy at Ω. The spectra of the time series in figure 12(*b*) has the peak at $\omega_0 - \Omega/2$ with two sidebands shifted by $\pm\Omega$. Similar data are recorded for $a = 1.13$ and $a = 1.30$ (Tran 1996).

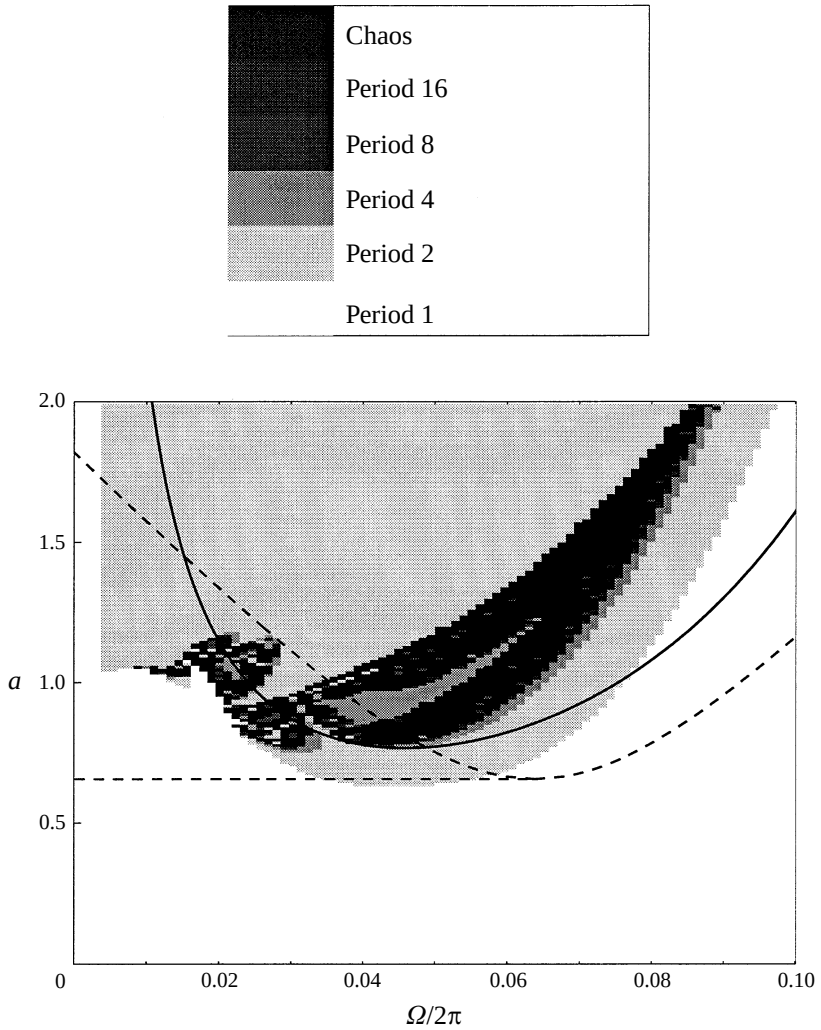

FIGURE 13. Predicted bifurcation scenarios for basin model, $W = 0$. Shaded areas: numerical simulation; dashed curves: approximate thresholds for period doubling; solid curve: Melnikov threshold.

7. Numerical bifurcation scenarios

7.1. *Homoclinic tangles* $W = 0$

Comprehensive numerical simulations have been performed for $-1 < W < 1$ to cover the important part of the parameter plane of a vs. σ ($\propto \Omega$). To see the overall picture, the various scenarios for $W = 0$ are typical and are summarized in figure 13. To facilitate comparison with experiments, numerical integration is first carried out in non-dimensional coordinates; the results are then transformed to physical coordinates via

$$\frac{\overline{A'}}{\tilde{A'}} = a \equiv \frac{\overline{A}_2}{\tilde{A}_2}, \qquad \Omega = \sigma\omega_0 c_F \frac{\overline{A'}}{b'}. \tag{7.1}$$

The lowest threshold for period-doubling bifurcation is seen to be at $\Omega/2\pi = 0.040$ Hz. The region of chaotic motion appears in a band bounded from both

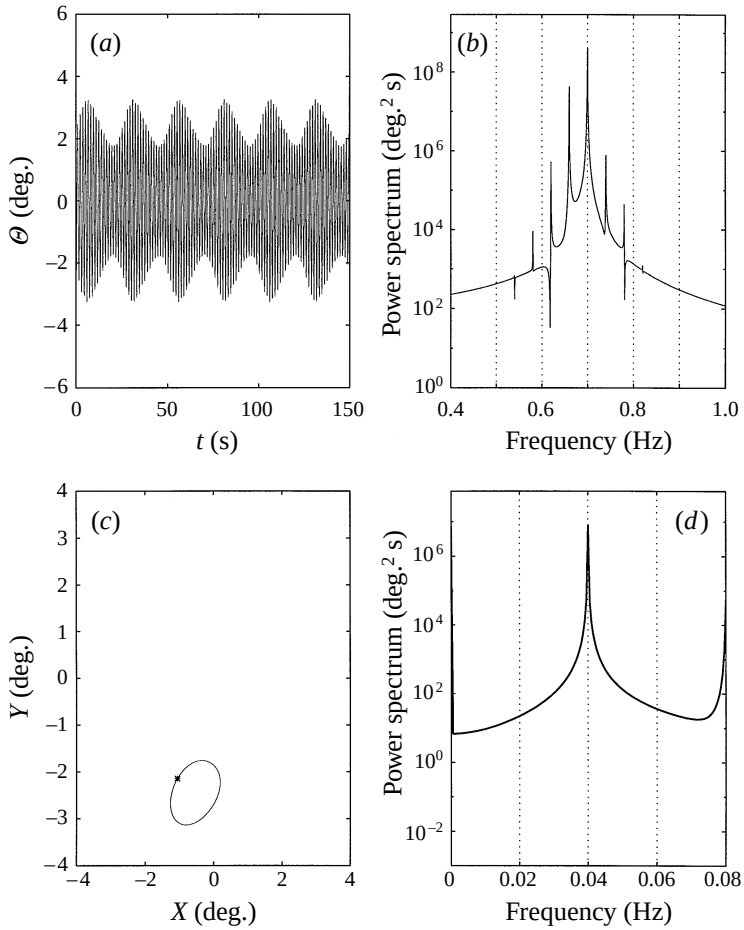

FIGURE 14. Computed gate response for $\Omega/2\pi = 0.04$ Hz, $a = 0.47$. Synchronous response. (*a*) Time series of gate rotation; (*b*) spectrum of gate rotation; (*c*) Phase trajectory and Poincaré map of gate envelope; (*d*) spectrum of envelope.

above and below by subharmonic responses. There is a thin strip of period-four response, embedded in a wider band of chaos, for modulational frequencies ranging approximately from 0.032 to 0.06 Hz. The numerical thresholds for period-doubling and for global chaos are in qualitative agreement with the approximate analytical thresholds given by multiple-scales and Melnikov's method respectively. Similar charts have been obtained by Sammarco (1996) for different values of α, β, γ and W.

We next present the details of numerical integration of the dynamical system (2.4) by fixing the modulational frequency at $\Omega/2\pi = 0.040$ Hz for which measurements have been described in the previous section. The computed time series of the envelope $X(T), Y(T)$ is first transformed to a time series of the gate rotation $\Theta'(t')$ by using the definition (1.4) of $\vartheta = X + \mathrm{i}Y$:

$$\Theta'(t') = \left(\frac{c_F \overline{A}'}{c_N b'}\right)^{1/2} (X + \mathrm{i}Y)\, \mathrm{e}^{-\mathrm{i}\omega t'} + * = \left(\frac{c_F \overline{A}'}{c_N b'}\right)^{1/2} 2\left[X(t')\cos\omega t' + Y(t')\sin\omega t'\right]. \tag{7.2}$$

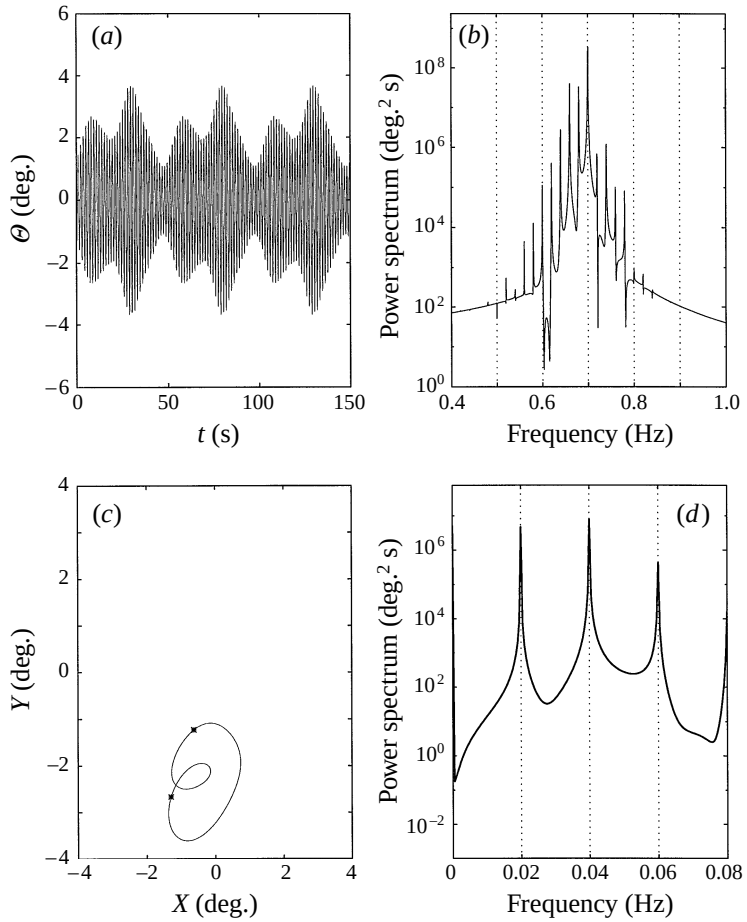

FIGURE 15. As figure 14 but for $a = 0.67$; subharmonic response.

Since the detuning of the carrier wave is chosen to be zero, $W = 0$, in (7.2) $\omega = \omega_0$. Computed results for increasing a are plotted in groups of figures. In each group (a) gives time series (7.2) of gate displacement, (b) the spectrum of (7.2), (c) the phase-plane trajectories of the envelope in X, Y, and the Poincarè map marked by a cross, and (d) the spectrum of the envelope X. The Poincaré map is obtained by sampling the time series of the envelope after every interval of $2\pi/\Omega$.

For $a = 0.47$ the response is synchronous, as can be seen in figure 14. The results are similar to the observed ones shown in figure 8. Note, in this and following graphs, there is a common feature of all the spectra shown in (b): the left sidebands are consistently larger than the right sidebands. This agrees with the observed data and appears to be an inherent feature of the Landau–Stuart equation.

Theoretically, for small amplitude a, there are two coexisting limit cycles in the Cartesian phase plane X, Y. They lie symmetrically with respect to the origin of the phase plane and represent oscillations of period $2\pi/\Omega$ around the fixed points $s_{1,2}$ of figure 1(e). A trajectory tends to one or the other depending on the initial conditions. The corresponding two time series of the angular displacement are identical but for a phase shift equal to π.

The threshold of period doubling is found numerically to be at $a = 0.57$. When

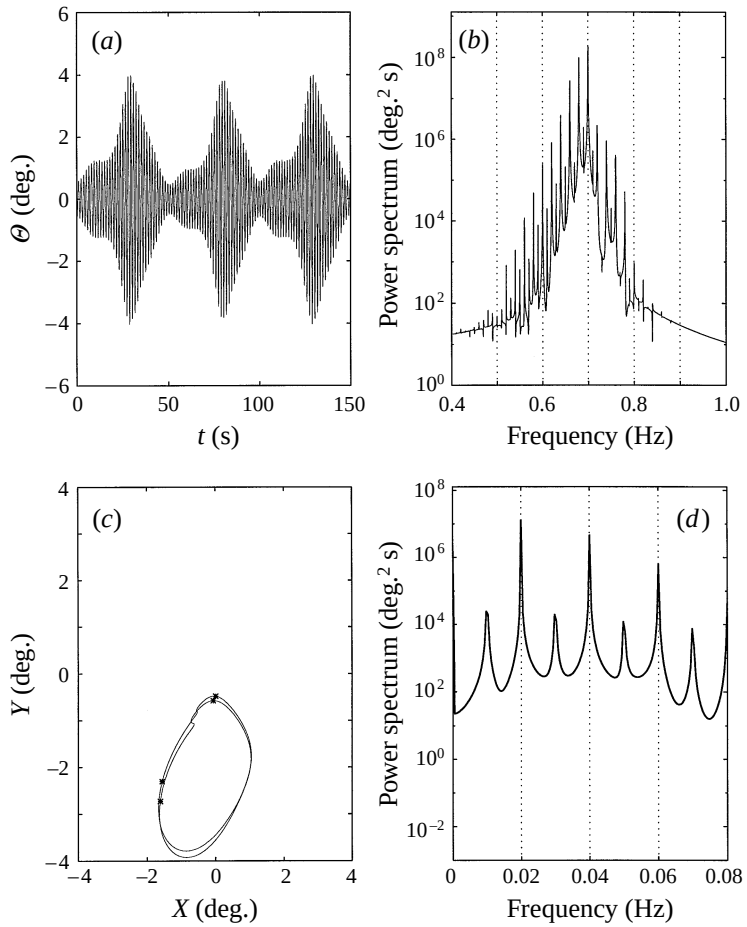

FIGURE 16. As figure 14 but for $a = 0.77$. Period-four response.

the modulational amplitude is increased to $a = 0.64$, subharmonic resonance is fully developed. We show in figure 15 the results for $a = 0.67$. In (b) the sidebands at $(\omega_0 \pm \Omega/2)/2\pi = 0.7 \pm 0.02$ Hz are strong, as in (d) at $(\Omega/2)/2\pi = 0.02$ Hz. These features are the same as those seen in the experiments for $a = 0.57$, as shown in figure 9. The period-doubled envelope bifurcates to a period-four orbit when $a = 0.77$. In figure 16(b) a small peak is born at $\omega_0 \pm \Omega/4$ and in (c) four fixed points appear in the Poincaré map. In (d), the subharmonic at $\left(\Omega/4\right)/2\pi = 0.01$ Hz is evident.

Chaos is fully developed when $a = 0.81$, as can be seen in figure 17. The spectrum in (b) maintains its peak at ω_0 but is broad-banded. In (c) the strange attractor spreads across the origin, which is a saddle point, to all four quadrants of the phase plane. Note that the S-shaped skeleton of the strange attractor resembles strongly the homoclinc orbit in figure 1(e), indicating the effect of homoclinic tangle, i.e. infinite transverse intersections of the stable and unstable manifolds near the homoclinic connection of figure 1(e).

For $a = 0.87$, figure 18 shows that chaos is replaced by period quadrupling with a downshift of the central spectral peak by $\Omega/4$, as is clearly shown in (b), (c) and (d).

When a is increased to $a = 0.97$, chaotic motion reappears, as shown in figures

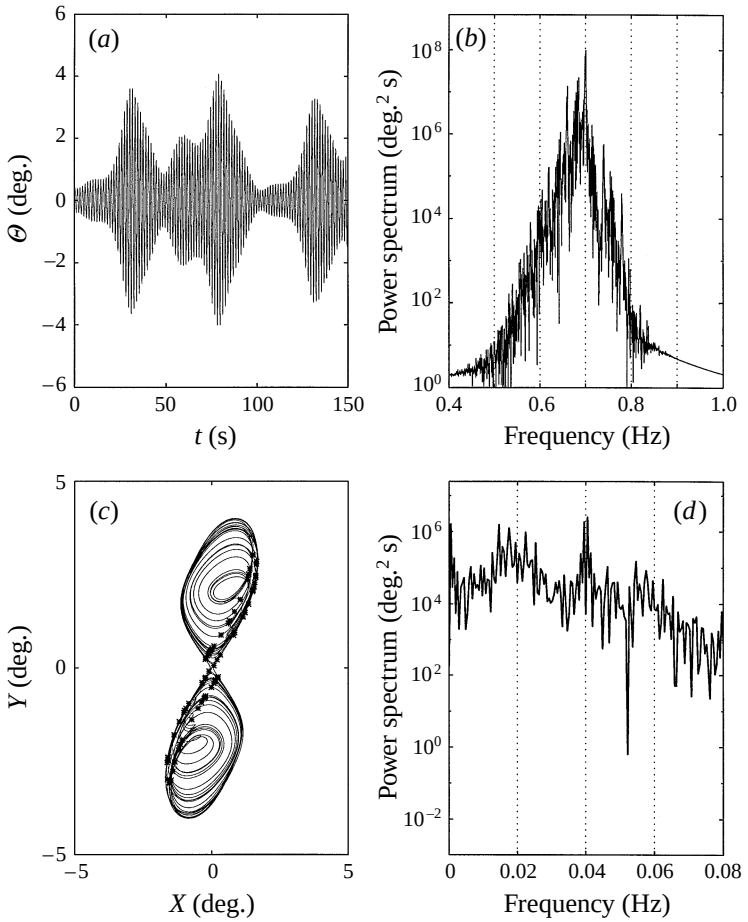

FIGURE 17. As figure 14 but for $a = 0.81$. Chaotic motion.

19(b) and 19(d) . The maximum energy is still around $\omega_0 - \Omega/4$. With further increase of a, the spectral peak shifts down to $(\omega_0 - \Omega/2)/2\pi = 0.68$ Hz.

For $a = 1.07$, chaos disappears again while frequency downshift is complete. Figure 20(a) shows that the modulation is strictly periodic while (b) shows the frequency peak at $\omega_0 - \Omega/2$, corresponding to the complete depletion of energy at ω_0 in (d). The closed trajectory in (c) is symmetrical with respect to the origin. For larger modulational amplitudes a, the response remains subharmonic in the envelope, with the peak shifted by $\Omega/2$ and increasingly larger phase trajectory in the (X, Y)-plane. The shape and size of the phase portraits are close to those observed experimentally (cf. figure 12 for $a = 1.03$).

The scenario depicted in figures 14 to 20 is typical of numerical simulations at other frequencies for different ranges of a (Sammarco 1996).

In summary, the theory largely confirms the laboratory observations, although not always at precisely the same modulational amplitudes. In particular the observed sequence of bifurcations leading to aperiodic motion is found in the numerical simulations, and the phase-plane geometries of period-doubled orbits and strange attractors essentially reproduced. In all the experimental spectra the left sideband is always larger than the right sideband; this is confirmed by the theoretical computations.

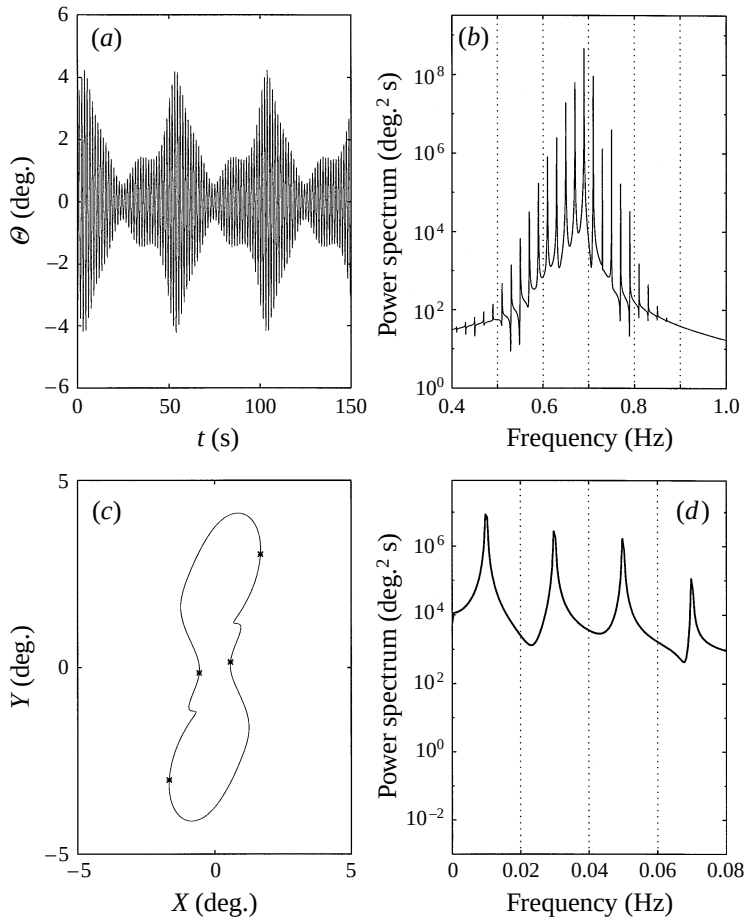

FIGURE 18. As figure 14 but for $a = 0.87$. Period-four and downshift by $(\Omega/4)/2\pi = 0.01$ Hz.

Moreover, when the modulational wave amplitude a is sufficiently large, the observed downshift of the central peak of the response is again predicted.

Better agreement would require experiments in a much larger wave basin, since spurious standing waves have been observed along the wavemakers and on the incidence side far from the gates. Such cross-waves result from reasonably large incident waves (hence nonlinearity) at certain frequencies within the range of our interest. In addition, rounding of gate corners to reduce damping implies a certain discrepancy between the theoretical and experimental geometries, which may also contribute to the discrepancies that remain between numerical predictions and observed data. Needless to say, the realm of the Landau–Stewart equation is limited in its range of time and amplitude; a more fully nonlinear theory would also reduce the remaining discrepancies.

7.2. *Heteroclinic tangles, $W = -1.5$*

The dynamics for $W < -1$ involves heteroclinc tangles and is more complex, and difficult to study in our laboratory. Figure 21 summarizes the numerical bifurcation scenarios for $W = -1.5$. The Melnikov threshold for the upper (lower) heteroclinic orbit is shown by the solid (dashed) curve. For low frequencies (< 0.06 Hz), period

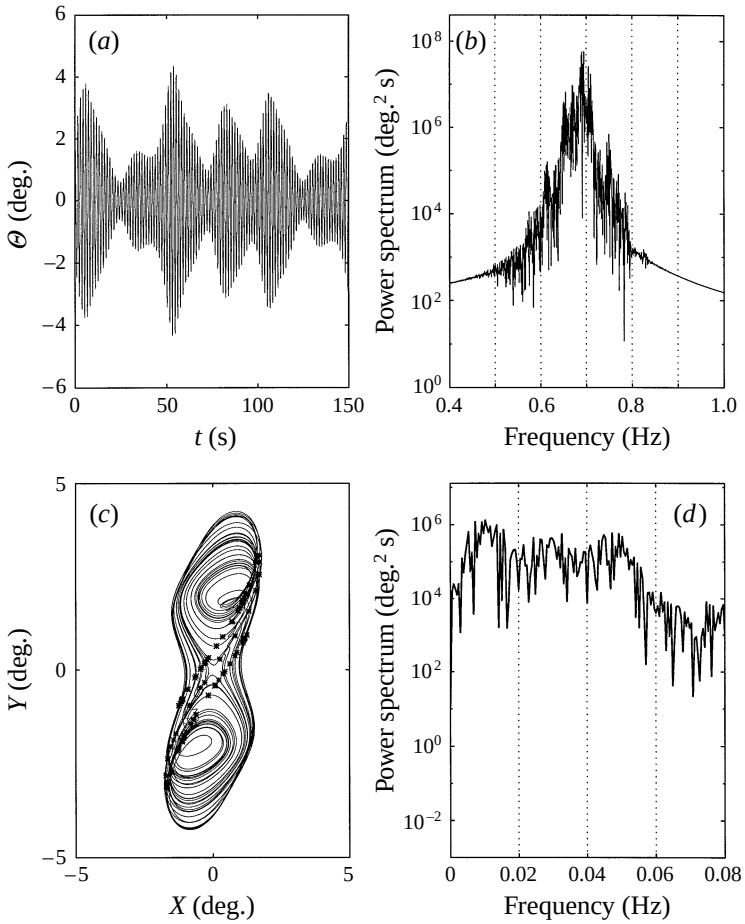

FIGURE 19. As figure 14 but for $a = 0.97$, chaotic motion.

doubling and chaos occur for a considerably above the predicted threshold for heteroclinic tangles (solid line). The region of chaos is limited in size and chaotic motion does not occur at all for very low frequency. This is consistent with the known fact that the Melnikov threshold for horshoe tangles is a necessary but not always a sufficient condition for global chaos (Moon, Cusumano & Holmes 1987). For higher frequency (> 0.06 Hz) chaotic behaviour occurs only for relatively large a, and is closer to the Melnikov threshold for the upper orbit (solid line).

In these numerical simulations, both trivial and non-trivial limit cycles are possible; the solution settles in several cases on the trivial state. Indeed in figure 21 the entire period-1 region above the band of chaotic response is the trivial solution.

Sample phase trajectories and resulting Poincaré sections are shown for $W = -1.5$ in figures 22(a, b, c) and 22(d, e, f) respectively. Figures 22(a) and 22(d) correspond to the point in the parameter plane of figure 21 $\{\Omega/2\pi,\ a\} = \{0.023,\ 1.29\}$, for which global analysis suggest that only the lower heteroclinc orbit tangles. Figures 22(b) and 22(e) are for $\{\Omega/2\pi,\ a\} = \{0.045,\ 2.67\}$, where global analysis admits horseshoe tangles for both lower and upper heteroclinic orbits. Finally figures 22(c) and 22(f) are for $\{\Omega/2\pi,\ a\} = \{0.12,\ 2.67\}$ where instead tangles occur only for the upper orbit. In this last case the phase trajectory never crosses the X-axis, a feature common to

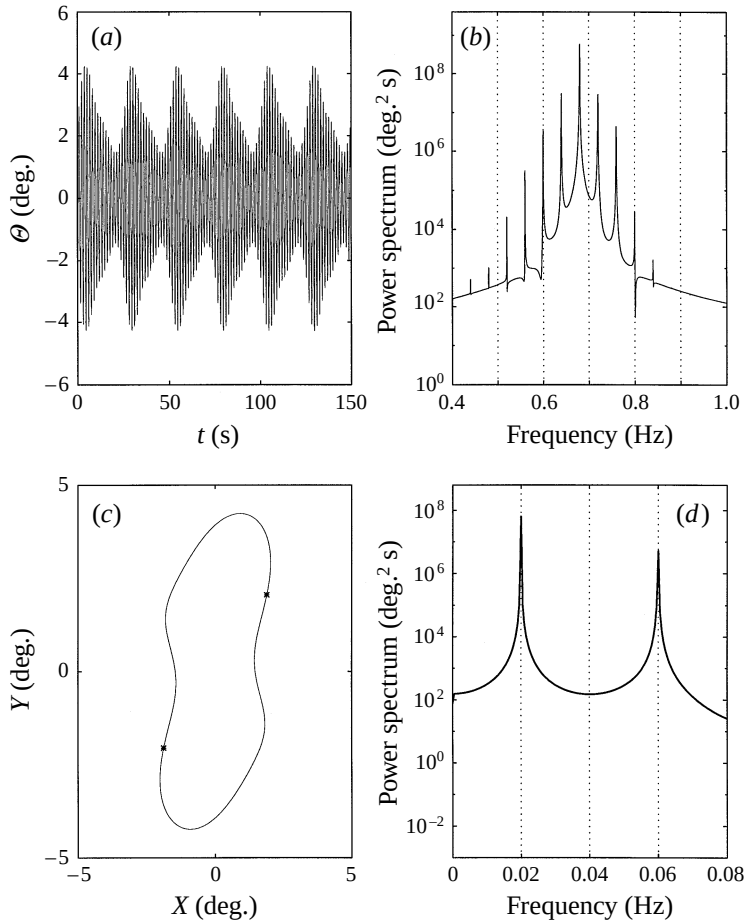

FIGURE 20. Computed gate response for $\Omega/2\pi = 0.04$ Hz, $a = 1.07$. Downshift is complete. (*a*) Time series of gate rotation; (*b*) spectrum of gate rotation; (*c*) phase trajectory and Poincaré map of gate envelope; (*d*) spectrum of envelope

all the strange attractors belonging to the band of chaos for $\Omega/2\pi > 0.07$ of figure 21.

8. Conclusions

To see the effects of finite bandwidth of the incident sea waves on the subharmonic resonance of the proposed Venice gates, we have considered the simplest model of a narrow-banded spectrum. The amplitude of the incident wave is periodically modulated in time. As a consequence the evolution equation for the envelope of gate oscillations becomes a second-order non-autonomous dynamical system. For small damping and wave modulation, local bifurcations are analysed by multiple-scale approximations to investigate modulational resonances. The prelude to chaos is analysed by the Melnikov method for Smale's horseshoe tangles of either homoclinic or heteroclinic orbits in the phase plane. The approximate criteria for local and global bifurcations give preliminary guidance for experiments.

Extensive numerical investigation of the above parameter plane corroborates with

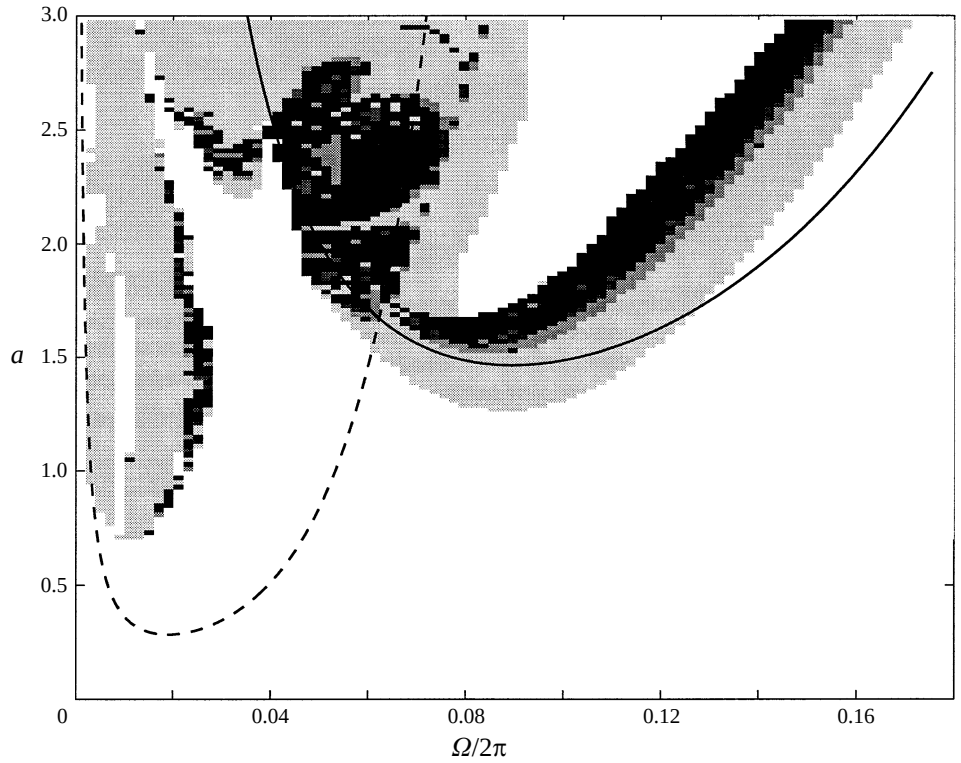

FIGURE 21. Predicted bifurcation scenarios for basin model, $W = -1.5$. Shaded areas: numerical simulation; solid curve: Melnikov threshold for upper heteroclinic orbit; dashed curve: Melnikov threshold for lower heteroclinic orbit.

the analytical predictions, and further delineated the regions of period quadrupling and chaos.

For a fixed modulational frequency in the incident sea, hence sideband width from the carrier wave, the general picture of the gate envelope can be summarized as follows. For a wavetrain with small periodic modulation a, the gate envelope is synchronous with the wave modulation. Increase of a induces bifurcations through a sequence of period doublings until modulational chaos is attained. For higher a above a band of chaos, the gate envelope returns to the state of subharmonic resonance, which is distinguished from the period doubling at lower a by a phase orbit symmetric about the origin. In the spectrum of the gate rotation, this state corresponds to a downshift of the central frequency from half the incident carrier wave of a quantity equal to half the modulational frequency. The response here is much larger than the non-resonant response to the same modulational wave amplitude but at a larger modulational frequency.

Numerical findings indicate that for sufficiently high frequency of modulation, no temporal resonances of any kind are possible. This means that large sidebands do not alter the resonance phenomenon induced by the carrier wave frequency. Specifically the period-doubling bifurcation route to chaos occurs only in sufficiently narrow wave sidebands, i.e. when the normalized separation σ of the sidebands from the central peak is around twice the natural frequency of the envelope $\lambda = 2(1 - W)^{1/2}$. For increasingly positive detuning of the carrier wave, i.e. as $W \to 1$,

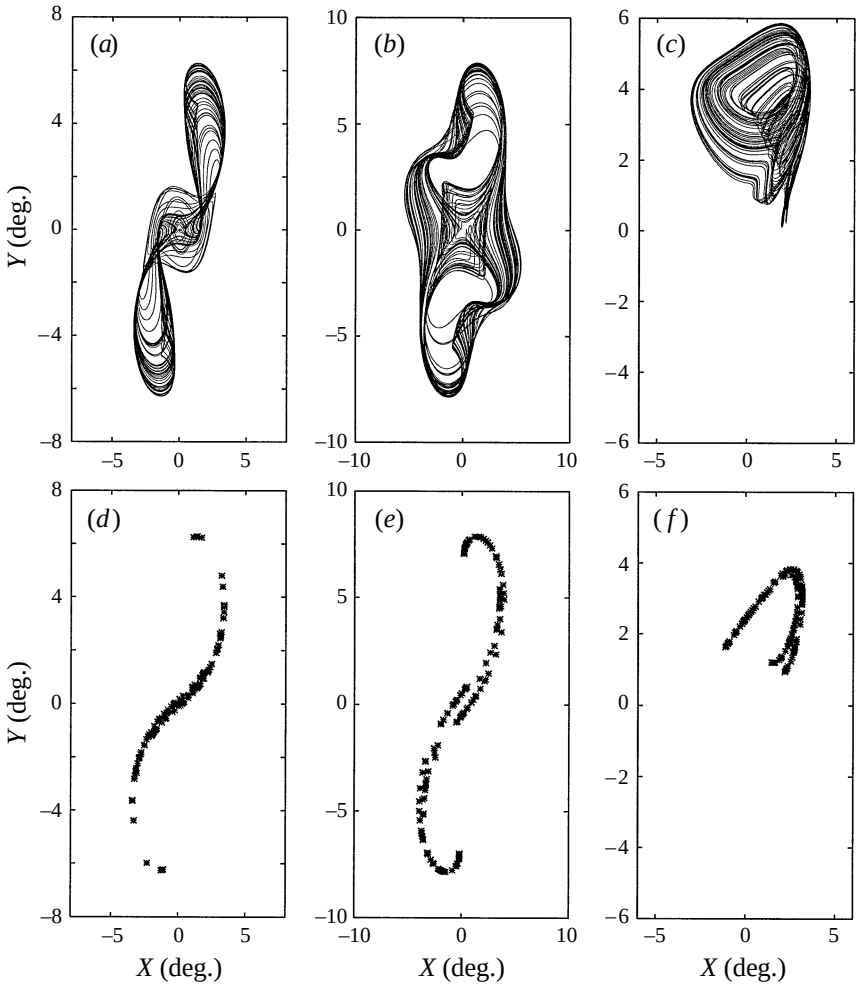

FIGURE 22. Sample strange attractors for $W = -1.5$. (a, b, c) Phase-plane trajectories. (d, e, f) Poincaré sections. (a, d) $\Omega/2\pi = 0.023$ Hz, $a = 1.29$. (b, e) $\Omega/2\pi = 0.045$ Hz, $a = 2.67$. (c, f) $\Omega/2\pi = 0.12$ Hz, $a = 2.47$.

modulational instability occurs for sidebands increasingly close to the central peak, and over a much longer time scale. On the other hand, as W decreases (negative detuning $\Delta\omega$), the thresholds for homoclinic or heteroclinic tangles and period doubling increase significantly. These findings should be helpful in the gate to avoid unwanted resonances.

In the present study, attention has been limited to a single mode. It is known in other physical contexts that chaotic motion can occur as a consequence of nonlinear interaction between adjacent modes (Ciliberto & Gollub 1984 for Faraday waves, or Mei & Zhou 1991 for bubble resonance by sound). Since adjacent gate modes can be close according to the linearized theory of Mei *et al.* (1994), modal interaction is an aspect worth investigating both theoretically and experimentally.

In the proposed design, the Venice gates are inclined at 50° from the horizon. It is likely that gate evolution equation will remain of Landau–Stuart type. However, both the first-order theory for the trapped modes, and the higher-order theory for

computing the coefficients of the Landau–Stuart equation must require the numerical solution of a number of wave–body interaction problems.

Finally, the effects of long-scale modulation along the barrier may require the study of a nonlinear Schrödinger equation with a time-dependent coefficient; the likelihood of spatial-temporal chaos should be interesting. Neglected in the present study, the difference in mean sea levels on two sides of the barrier in a storm also warrant additional efforts in the future.

We thank Professor Alberto Noli, University of Rome, and Professor Attilio Adami, University of Padua, for their encouragement which initiated the authors' interests in this problem. Funding has been provided by grants from US Office of Naval Research (Accelerated Research Initiative on Nonlinear Ocean Waves directed by Dr T. Swean (Grants Nos. N00014-92-J-1754, and N00014-95-1-8040 (AASERT)), US National Science Foundation (Grants Nos. CTS-9115689 and CTS 9634120) directed by Drs S. Traugott and R. Arndt, and Consorzio Venzia Nuova for laboratory equipments.

REFERENCES

Agnon, Y. & Mei, C. C. 1985 Slow-drift motion of a two-dimensional block in beam seas. *J. Fluid Mech.* **151**, 279–294.

Ciliberto, S. & Gollub, J. P. 1985 Chaotic mode competition in parametrically forced surface waves. *J. Fluid Mech.* **158**, 381–398.

Guckenheimer, J. & Holmes, P. 1983 *Nonlinear Oscillations, Dynamical Systems, and Bifurcations of Vector Fields*. Springer.

Jiang, L., Ting, C., Perlin, M. & Schultz, W. W. 1996 Moderate and steep Faraday waves instabilities, modulation and temporal asymmetries. *J. Fluid Mech.* **329**, 275–307.

Jordan, D. W. & Smith, P. 1986 *Nonlinear Ordinary Differential Equations.* Clarendon.

Lo, E. & Mei, C. C. 1985 A numerical study of water-wave modulation based on a higher-order nonlinear Schrödinger equation. *J. Fluid Mech.* **150**, 395–416.

Mei, C. C., Sammarco, P. Chan, E. S. & Procaccini, C. 1994 Subharmonic resonance of proposed storm gates for Venice Lagoon. *Proc. R. Soc. Lond.* A **444**, 463–479.

Mei, C. C. & Zhou, X. 1991 Parametric resonance of a spherical bubble *J. Fluid Mech.* **229**, 29–50.

Melville, W. K. 1983 Wave modulation and breakdown. *J. Fluid Mech.* **128**, 489–506.

Moon, F. C., Cusumano, J. & Holmes, P. J. 1987 Evidence for homoclinic orbits as a precursor to chaos in a magnetic pendulum. *Physica* **24D**, 383–390.

Sammarco, P. 1996 Theory of subharmonic resonance of storm gates for Venice Lagoon. PhD thesis, MIT, Dept. of Civil & Environmetal Engineering.

Sammarco, P., Tran, H. H. & Mei, C. C. 1997 Subharmonic resonance of Venice gates in waves. Part 1. Evolution equation and uniform incident waves. *J. Fluid Mech.* **349**, 295–325.

Tran, H. 1996 Experiments on subharmonic resonance of storm gates for Venice Lagoon. *MS thesis, MIT, Dept. of Civil & Environmetal Engineering.*

Trulsen, K. & Mei, C. C. 1995 Modulation of three resonanting gravity–capillary waves by a long gravity wave. *J. Fluid Mech.* **290**, 345–376.